Experimental study into the effect of wind-ice misalignment on the development of ice-induced vibrations of offshore wind turbines
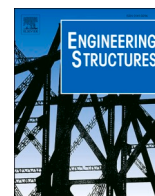
Hammer, Tim C.; Hendrikse, Hayo

Important note
To cite this publication, please use the final published version (if applicable).
Please check the document version above.

Experimental study into the effect of wind-ice misalignment on the development of ice-induced vibrations of offshore wind turbines

Tim C. Hammer [a,b,*], Hayo Hendrikse [a]

[a] Delft University of Technology, Faculty of Civil Engineering and Geosciences, Department of Hydraulic Engineering, Stevinweg 1, 2628 CN Delft, the Netherlands
[b] Siemens Gamesa Renewable Energy, Prinses Beatrixlaan 800, 2595 BN Den Haag, the Netherlands

ARTICLE INFO

ABSTRACT

The effect of misalignment between wind- and ice loading direction on the development of ice-induced vibrations of offshore wind turbines has been investigated experimentally. In the experiments a hybrid test setup was used to study the structural response to combined loading from physical model ice and numerically applied wind. The motivation for this study was the high uncertainty in the design of offshore wind turbine support structures in cold regions, caused by scarcity of full-scale and model-scale data on ice-structure interaction. Test results revealed that misaligned scenarios result in the development of sustained ice-induced vibrations in the ice load direction. The test results also showed that ice-induced vibrations can develop up to higher ice drift speeds for misaligned scenarios than for aligned scenarios. Both observations are considered to be related to low total damping in the ice drift direction for a misaligned scenario. Further comparison between a 90°-misaligned operational and an aligned idling scenario revealed that wind-induced structural displacements perpendicular to the ice drift direction do not cause the ice to fail. On the contrary, it was shown that the ice constrains the wind-induced motion for low relative velocities between ice and structure. For high relative velocities, wind-induced displacements approach those in open water as the ice fails in rapid succession at the sides of the structure during crushing. The analysis of a misaligned scenario with a smaller misalignment angle revealed that vibrations occur perpendicular to the ice drift direction and are characterized by relatively low amplitude and high frequency. The ice, being in contact with the structure, neither prevented those vibrations nor failed.

1. Introduction

Ice-induced vibrations of offshore structures are an important design consideration. Ice-induced vibrations are caused by an interaction between crushing ice and structures with a vertical face at the ice-action point. In the past, ice-induced vibrations of offshore structures have been recorded for structures in the Cook Inlet [1,2] and Bohai Sea [3], lighthouses [4,5], channel markers [6] and the Molikpaq platform [7]. The LOLEIF ("Validation of LOw LEvel Ice Forces") project [8] and the follow-up STRICE ("measurements on STRuctures in ICE") project [9] instrumented the Norströmsgrund lighthouse for data collection on ice loads and ice-induced vibrations. Several model-scale tests were conducted to reproduce and analyse the development of ice-induced vibrations of specific structures such as the JZ-20–2 jacket platform [10], the Great Belt West bridge [11,12], and the Molikpaq structure [13,14]. Other model-scale tests focussed on the general development of ice-structure interaction, validation of numerical models and derivation of

dimensionless numbers for prediction of ice-induced vibrations instead [15–23].

Nowadays, structures such as offshore wind turbines are installed in cold regions, including the Baltic Sea and Bohai Bay. The susceptibility of offshore wind turbines to ice-induced vibrations is expected to differ significantly from that of offshore structures which had experienced ice loads in the past. The reason is that offshore wind turbines have relatively low natural frequencies in combination with a slender interface at the ice-interaction point. Also, offshore wind turbines experience significant wind loads in addition to ice loads acting on the structure. Those wind loads can act directionally misaligned to the ice load direction, potentially influencing the development of ice-induced vibrations. Multidirectional, environmental loading of offshore wind turbines is commonly considered when wind and wave loading is addressed [24]. In the case of wind and ice loading, this is far less common, and it is often assumed that ice and wind act on the structure from the same direction while studies of sea ice dynamics suggest differently [25]. Focussing for

---

* Corresponding author.
  E-mail address: t.c.hammer@tudelft.nl (T.C. Hammer).

example on the Baltic Sea, the region with the most ongoing and planned offshore wind developments with seasonal sea ice, deviation angles (here: misalignment angles) typically vary between 22° and 30° [25,26]. These misalignment angles are related to site-specific currents, and Coriolis and tilt effects that act directly on the ice independently of the wind direction. Additionally, high inertia of the ice prevents it from quickly following changes in wind direction. As a result, misalignment angles between wind and ice of up to 90° can be observed in the data collected during the STRICE campaign in the Baltic Sea [27,28].

Unfortunately, public full-scale data of an offshore wind turbine loaded by ice only exist for foundations with cones at the ice action point [29,30]. As no full-scale data of ice-induced vibrations of offshore wind turbines with a vertical interface at the ice action point exist, numerical models, which have been implemented for industry purposes [31,32], have to be validated by a combination of model-scale data and full-scale data from structures other than wind turbines. Model-scale tests of offshore wind turbines in ice have typically been based on single-degree-of-freedom structures with high natural frequencies [33–37] and have suffered from mixed failure modes of the ice at low ice drift speeds (e.g., [23,33,37]). A first attempt to test ice-induced vibrations of a multi-degree-of-freedom representation of an offshore wind turbine in model ice was recently published in [38]. The authors applied wind loading in the numerical domain of their hybrid test setup to reproduce operational load scenarios. However, these experiments focussed on aligned conditions between wind and ice only.

So far it has been neither experimentally nor numerically investigated how a misaligned wind-ice scenario affects the development of ice-induced vibrations of an offshore wind turbine. Furthermore, it is currently unknown how wind-induced structural displacements originating from the tower and rotor-nacelle-assembly interacting with the wind would impact the development of ice-induced vibrations.

Herein we present the results of an experimental study into the effects of wind-ice misalignment on the development of ice-induced vibrations for an offshore wind turbine on monopile foundation.

We expected that misaligned scenarios result in a different ice-structure interaction compared to aligned scenarios. The reason for this expectation is that the aerodynamic damping, which may mitigate the development of ice-induced vibrations, has a much smaller effect on the ice-structure interaction when the ice acts in a different direction from the wind. In addition, we expected that the wind-induced displacement and corresponding force would crush the ice in wind load direction, thereby influencing the development of ice-induced vibrations.

The focus of the experiments and analysis lays on the effects of wind-ice misalignment on the resultant ice loads and structural displacements at the ice action point. We compare a 90°-misaligned operational scenario with an aligned idling scenario in an attempt to separately assess the effect of wind-induced motion perpendicular to the ice drift direction on the ice loads, structural displacement, and spatial distribution of the ice load. We then analyse the effect of structural motions due to an applied predefined wind loading on the ice-structure interaction. The results, reliability of the data and generalisation of results are discussed. Note that the term 'ice' as used in the study is a replacement for first-year sea-ice, as we consider seasonal ice regions such as the Baltic Sea.

2. Experimental campaign

To guarantee ice failing in crushing against a model-scale structure with low natural frequencies, the SHIVER ("An advanced ice model for application in design of offSHore wind turbines susceptible to Ice-induced Vibrations based on model-scale expERiments") project applied a hybrid test method in cold model ice [39]. Raw experimental data can be obtained from [40]. The project recorded ice-induced vibrations such as intermittent crushing, frequency lock-in and continuous brittle crushing and revealed a new multi-modal ice-induced vibration regime for offshore wind turbines [38,41]. Intermittent crushing is

defined as a quasi-static interaction regime, characterized by a 'sawtooth load and response pattern' including significant load drops after long phases of relative low velocity between the structure and the ice. Multimodal interaction is characterized by an amplified response in multiple structural modes due to interaction with the ice. Frequency lock-in presents itself as a quasi-harmonic structural response with a frequency close to one of the natural frequencies of the structure. Both multi-modal interaction and frequency lock-in result in periodicity in the ice load signal. Continuous brittle crushing is characterized by a low dynamic response to high frequency loading by the ice.

Because the hybrid test setup consisted of two electrical actuators, which were installed perpendicular to each other (see Section 2.2), the effect of simultaneous bi-directional loading of an offshore structure could be investigated in the present study. More specifically, the present study focusses on the misalignment of wind and ice loading direction and consequent effects on the development of ice-induced vibrations, targeting ice types which are typical for seasonal ice regions such as the Baltic Sea.

2.1. Scaling

Palmer and Dempsey [42] stated that "ice is best modelled by ice" once ice is failing in crushing. The reason for this statement is that appropriate scaling laws do not yet exist for crushing ice. Gravitational forces (Froude scaling) are negligible during the in-plane compression failure of ice. They further describe that, once the Froude scaling is rejected, the Cauchy scaling no longer requires a reduction in the ice strength. For the SHIVER test campaign, we thus attempted to test cold model ice with an ice strength (compression) as close to full-scale ice as practicable (replica modelling). The growing procedure of the cold model can be found in [39].

In addition, we planned to test with un-scaled structural response (length and time scaling factors of one). To obtain un-scaled responses while testing with scaled model-ice forces, it was required to scale structural properties respectively. The merits of such a scaling approach for ice-induced vibrations were recently discussed by Ziemer [43].

Ultimately, we chose to scale all properties with a single scale factor λ_m given as the ratio between a chosen full-scale mean brittle crushing load of 1.7 MN and expected model-scale mean brittle crushing load of 1 kN. The chosen factors resulted in a scale factor for the tests of $\lambda_m = 1700$ as described in detail in [38]. In the tests, we numerically applied a wind force at tower top which was scaled with the same factor as the ice loads λ_m. Physical quantities and their scaling factors are listed in Table 1 for clarification.

It is important to emphasize that we chose to relax the geometrical scaling requirements. We tested with a structural diameter (200 mm) and a target ice thickness (30 mm) which would guarantee that the ice

Table 1

Scale factors based on the scale factor λ_m. *The length scaling applies to response, not to geometry.

Physical quantity	Unit	Scale factor applied
General		
Length	[m]	1*
Time	[s]	1
Structure		
Frequency	[s]	1
Damping	[-]	1
Mass-normalized mode shapes	[kg$^{-0.5}$]	$\lambda_m{}^{-0.5}$
Aspect ratio		18.8 (full-scale) / 6.7 (model-scale)
Ice		
Strength	[N m^{-2}]	1
Ice drift speed	[m s^{-1}]	1
Mass	[kg]	not to scale
Brittle crushing force	[N]	λ_m
Wind		
Force	[N]	λ_m

would fail in crushing, avoiding mixed mode failure as observed in previous model-scale experiments. Also, effects of broken ice at the ice-structure interface were not captured accurately as broken ice typically slides freely over the intact ice surface due to low friction in model tests rather than resulting in a large rubble pile. When scaling the results to full-scale, there should be a provision made for the broken ice which typically results in an additional static load contribution. The loads from broken ice have been determined to be small compared to intact ice by Kärnä and Qu [9].

We attempted to verify the validity of this scaling approach by simulating two existing full-scale structures, as part of the experimental campaign, which have experienced ice-induced vibrations and from which full-scale data are available: the Molikpaq caisson and the Norströmsgrund lighthouse. Results of those tests give confidence to the scaling method, and at the same time reveal that certain aspects are not accurately captured, such as the fluctuation of the slow-varying mean ice load during continuous brittle crushing. For a more detailed assessment of these two scenarios and the scaling approach, the reader is referred to [44].

2.2. Test setup

For the present test campaign, a real-time hybrid test setup was used. The hybrid test setup solves a numerical model with the input from real-time physical measurements to determine the response of the physical test pile. The test setup used during the experimental campaign is shown in Fig. 1. Once the structural model (1) is implemented in the numerical solver (2), the carriage is moved and drags the physical setup through the ice to simulate the ice drift (3). Installed strain gauges inside the aluminium pile (4) were used to identify the ice load as input to the numerical model. The structural model was solved to obtain the displacements of the structure, which were then imposed by two electric actuators in real-time (5). The inherent delay in the system of 4.5 ms was compensated using a forward-prediction algorithm [45]. Further explanation about the measurement systems and verification of the

structural simulation method can be found in [46]. As two electric motion-controlled actuators were installed, one aligned with the direction of the moving carriage, and another one orthogonal to that direction, it was possible to consider structural responses due to multi-directional loading.

2.3. Structural model of the offshore wind turbine

During the test campaign the offshore wind turbine was not modelled in full, but rather a linearized modal model was used. The choice to not incorporate the full RNA and blade-wind interaction in the numerical part of the hybrid test setup was made as the expectation was that the most important effects on the ice-structure interaction would result from the added aerodynamic damping and the wind-induced motions of the support structure. The latter effects could be modelled with a simplified structural model. This implies that a full hybrid setup was not achieved here, though it is argued that effects of the non-linear interaction between wind and blades combined with the ice-structure interaction can be investigated in the numerical domain once an ice model has been established which accurately captures the effects observed in the test campaign.

Structural properties of the implemented offshore wind turbine model in the hybrid test setup are based on a 14 MW offshore wind turbine. The full offshore wind turbine model had been developed for numerical simulations of ice-structure interaction of offshore wind turbines in the Bonus Horizontal axis wind turbine Code (BHawC) from Siemens Gamesa Renewable Energy [38]. The offshore wind turbine is based on a (steel) monopile foundation and has a full-scale diameter of 7.5 m at mean sea level (MSL). The interface between tower and transition piece is at 14 m above MSL, the tower top is roughly at 134 m above MSL. The offshore wind turbine has been designed for a water depth of 30 m, resulting in the pile tip at 62 m below MSL. Scaled, linearized structural modal properties, as shown in Table 2, are derived by a modal analysis of a lumped mass model derived from the full offshore wind turbine model in BHawC. The structural frequency in
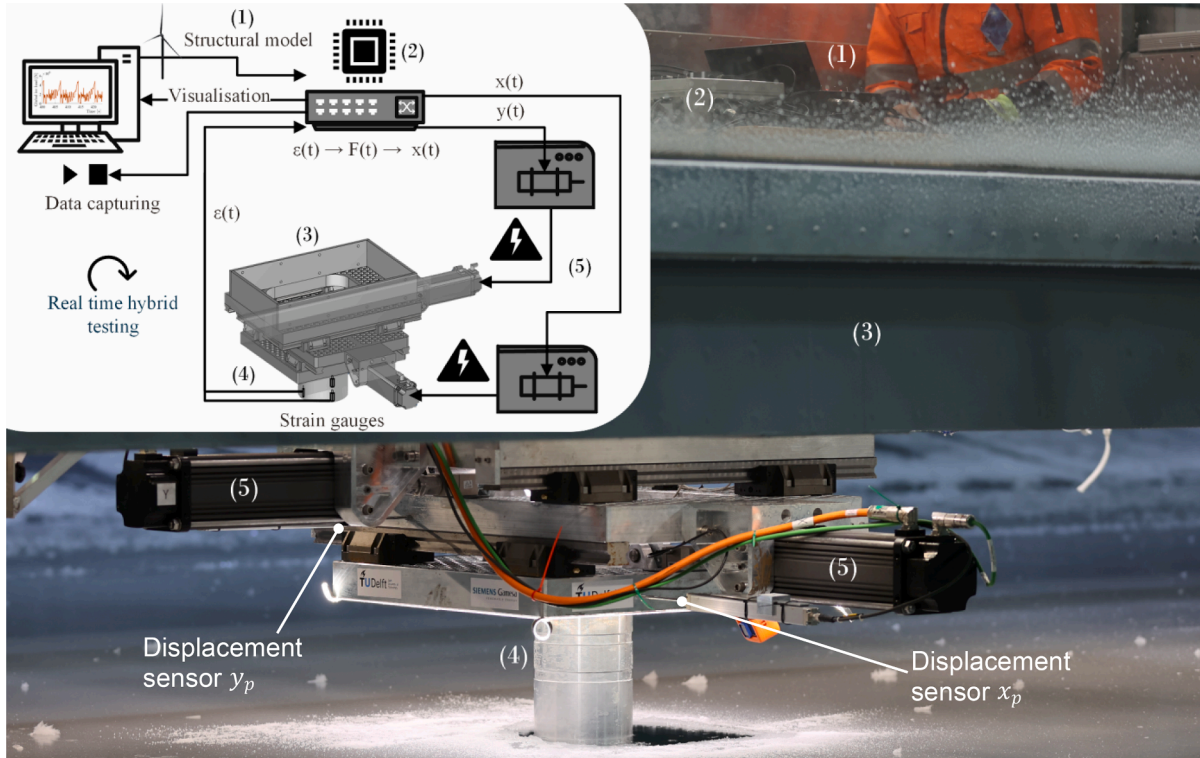

Fig. 1. Photograph of the hybrid test setup used during the experiments and a sketch of the components (top left).

Table 2
Scaled modal information at ice-structure interaction point (MSL) and tower top (TT) for the lumped mass model used to simulate the offshore wind turbine during the experiments. Subscripts *idl* and *oper* indicate idling and operational scenarios, respectively.

Mode	f	ζ_{idl}	ζ_{oper}	$\phi_{x, MSL}$	$\phi_{y, MSL}$	$\phi_{x, TT}$	$\phi_{y, TT}$
	[Hz]	[%]	[%]	$[10^{-3}$ kg$^{-0.5}]$	$[10^{-3}$ kg$^{-0.5}]$	$[10^{-3}$ kg$^{-0.5}]$	$[10^{-3}$ kg$^{-0.5}]$
1	0.153	0.8	1.0	−1.86	0.00	−39.10	0.00
2	0.154	0.8	10.2	0.00	1.88	0.00	39.39
3	0.824	1.2	1.8	12.66	0.00	52.14	0.00
4	0.888	1.3	4.4	0.00	−14.79	0.00	2.20
5	1.50	2.6	3.4	19.29	0.00	−10.55	0.00
6	1.66	1.9	5.9	0.00	−18.72	0.00	8.14
7	2.72	5.4	5.8	9.49	0.00	13.00	0.00
8	2.91	4.1	5.8	0.00	−7.53	0.00	−13.93
9	5.11	5.4	5.8	−9.39	0.00	−9.24	0.00
10	5.21	5.4	5.8	0.00	−10.04	0.00	−10.44
11	7.46	5.4	5.8	18.60	0.00	−7.25	0.00
12	7.54	5.4	5.8	0.00	18.54	0.00	−8.23
13	10.5	5.4	5.8	−2.35	0.00	−6.83	0.00
14	10.5	5.4	5.8	0.00	−1.95	0.00	−7.66
15	13.4	5.4	5.8	−16.12	0.00	−4.29	0.00
16	13.4	5.4	5.8	0.00	16.08	0.00	4.70
17	15.2	5.4	5.8	0.00	−7.03	0.00	−3.73
18	15.3	5.4	5.8	6.14	0.00	3.43	0.00
19	17.3	5.4	5.8	−9.17	0.00	4.98	0.00
20	17.3	5.4	5.8	0.00	8.70	0.00	−5.51

Table 2 is f, ζ_{idl} and ζ_{oper} are the damping in idling and operational load conditions, respectively, and ϕ is the mass-normalized mode shape amplitude at the mean sea level (MSL) and tower top (TT) in *x*- and *y*-direction.

2.4. Predefined wind fluctuation

To account for the wind in the experiments, we applied a (shaft) force as an external (predefined) force and added modal aerodynamic damping in wind direction in the numerical domain.

To generate a representative shaft force, we ran fully-coupled BHawC simulations. The simulations considered a wind shear law as defined in IEC 61400-1 [47]. The wind profile was defined for an averaged wind speed of 12 m s^{-1} at hub height, a reference height of roughly 139 m above MSL, a power law coefficient of 6, a roughness length of 0.09, and a turbulence intensity of 0.104. In addition, and as recommend by IEC 61400-1 [47], a uniform shear Mann turbulence model was applied. Aerodynamics were modelled by the blade element momentum theory and further applications as described in [38]. Finally, we extracted the shaft force in fore-aft direction at the hub flange. Note that we did not consider cross-directional shaft forces as the application would have unnecessarily complicated the analysis of ice-induced load effects in cross-direction. Only a portion of the extracted time series from

BHawC could be used because the microcontroller of the test setup had a limit of 2000 entries (i.e. 20 s at 100 Hz). We subtracted the mean shaft force to minimize the static deflection of the hybrid test setup, which would not affect the interaction with the ice. The shaft force time series subtracted by its mean is henceforth called wind fluctuation in the present study. As we tested for durations longer than 20 s, the predefined wind fluctuations are repeatedly applied at tower top (TT) as can be seen for a loading scenario without ice in Fig. 2. The figure presents post-processed structural displacements at the ice action point (here: MSL) in the wind load direction (here: *x*) for a 90°-misaligned scenario in an open-water experiment and compares those to numerically determined displacements. The wind load repetition cycle of 20 s can be observed, which was limited by the processing capacity of the microcontroller.

The linearized aerodynamic damping was determined by comparing the results of a modal analysis under operational condition for an averaged wind speed of 12 m s^{-1} and an idling condition in BHawC. The determined linearized aerodynamic damping is added to the modal damping in the direction of the applied wind fluctuations (Table 2, ζ_{aero} = ζ_{oper} - ζ_{idl}).

2.5. Definition of misalignment angles

During testing, the direction of indentation into the ice could not be changed. Coordinate transformations were therefore made in the numerical domain to account for wind-ice misalignment (Fig. 3). First, the measured ice load was projected on the structure coordinate system (x_s, y_s), after which the structure response was determined, combining both physical ice and numerical wind loading. The resulting response was converted back to the pile coordinate system (x_p, y_p) before being applied by the actuators. For example, measured ice loads in y_p-direction are applied in x_s-direction for a 90°-misaligned scenario ($F_{y_p} = F_{x_s}|_{\varphi=90°}$).

During the campaign misalignment angles of $\varphi = (0°, 30°, 90°)$ were tested. When not mentioned otherwise, the turbine tested was in operational mode (wind load fluctuations applied and aerodynamic damping added). For an idling scenario, neither wind load fluctuations were applied nor was aerodynamic damping added to the structural damping.

2.6. Test matrix and measurements

Test data used in the present study were collected on two different test days (17.06.2021 and 21.06.2021) and are listed in further detail in Table 3. Corresponding load scenarios are visualized in Fig. 4. Only four ice drift speeds for a 30°-misalignment scenario were tested. Focus on the lower range of speeds was set, as it was expected to see the most severe ice-induced vibrations for this range of ice drift speeds.

The ice during the two test days was kept at a temperature (T) of −11 °C to obtain crushing behaviour. The ice thickness h_{mean} during the tests is given as an average of four thickness measurements over the length of a test run. The compressive and flexural strength (σ_c, σ_f) were
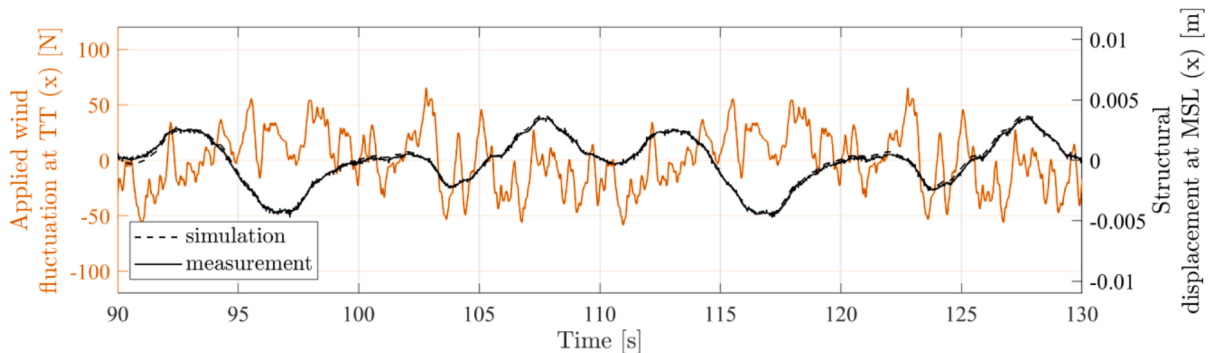

Fig. 2. Wind load fluctuations applied at tower top (TT) and wind-induced displacements of the structure at the ice action point (here: MSL) as numerically determined and measured in a test without ice present (Test ID 380 [35]).
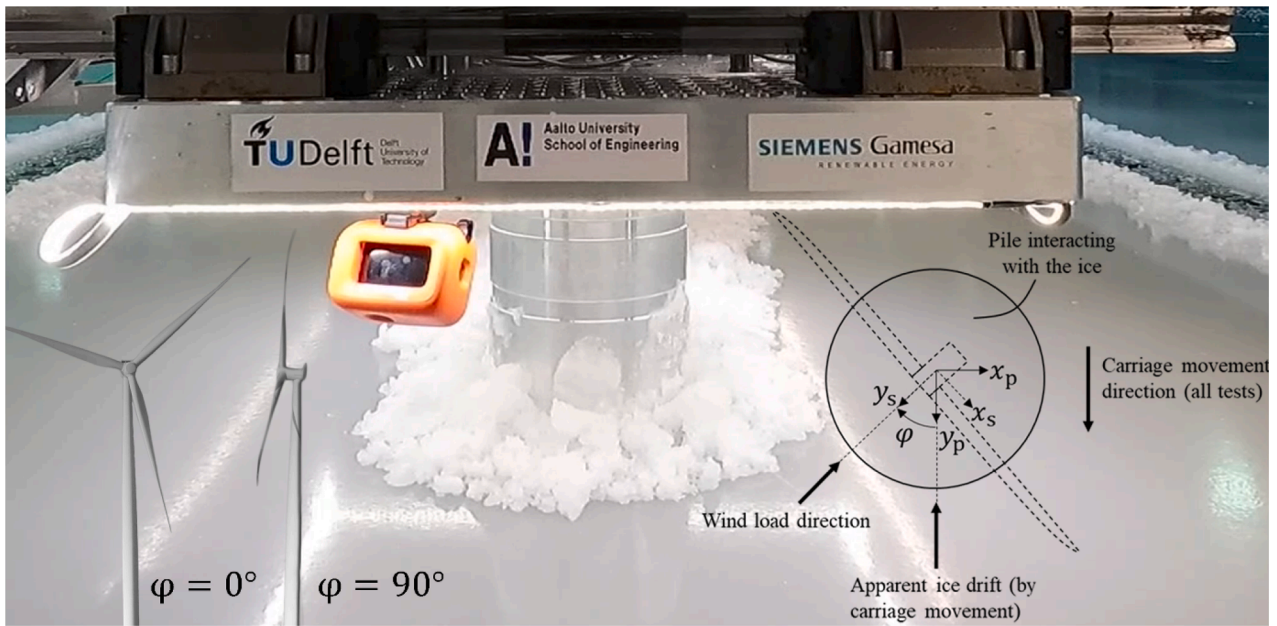
Fig. 3. Definition of wind-ice misalignment and corresponding coordinate systems used during the experiments.

Table 3
Overview of tests considered in the present study.

| Scenario	Test ID	Ice drift speed [mm s^{-1}]	Test day and run	T [°C]	σ_c [kPa]	σ_f [kPa]	h [mm]
0°	382, 383, 384, (385 + 577)	5, 10, 15, (20)	17.06.2021 Run 1	−11 °C	563	549	28
0°	401, (402 + 630), 403, 404	25, (30), 40, 50	17.06.2021 Run 5	−11 °C	563	549	28
30°	392, 393, (394 + 568), 395	5, 10, (15), 20	17.06.2021 Run 3	−11 °C	563	549	27
90°	387, 388, 389, 390	5, 10, 15, 20	17.06.2021 Run 2	−11 °C	563	549	30
90°	405, 406, 407, (408 + 631)	25, 30, 40, (50)	17.06.2021 Run 6	−11 °C	563	549	24
0°, Idling	590, (591 + 633), 592, 593	5, (10), 15, 20	21.06.2021 Run 3	−11 °C	579	526	31
0°, Idling	599, 600, 601, 602	25, 30, 40, 50	21.06.2021 Run 5	−11 °C	579	526	32
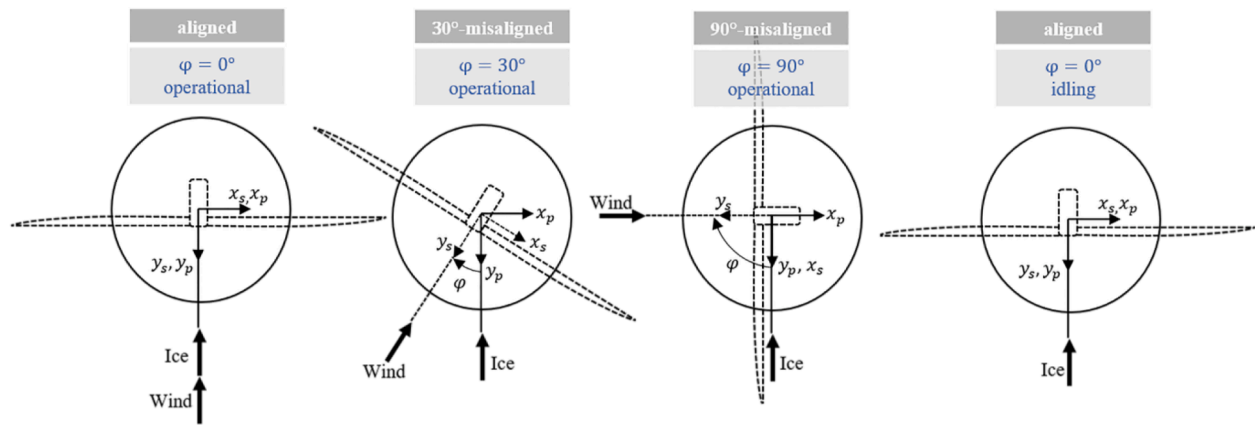
Fig. 4. Aligned and misaligned scenarios considered in the experiments.

measured once at the end of the test day. It is noted that the measurement beam bent when determining the compressive strength, thereby compromising the in-situ characterisation. The effect on σ_c listed here (Table 3) is unknown, but it may be that it was somewhat underestimated.

As an alternative material characterisation, we performed rigid

indenter tests at an ice drift speed of 0.1 mm s^{-1} on 21.06.2021, resulting in forces of up to 10kN for a contact area of 0.03 m × 0.2 m. This results in an effective pressure of 1.67 MPa which is about a factor three higher than the measured compressive strength and similar to full-scale ice. The effect of confinement on this measurement is at this point unknown, but it could imply that the strength of the ice is somewhat higher than measured using the standard property test. This topic is to be further investigated in a future campaign.

The present study analysed ice loads measured by strain gauges in the upper ring of the tested cylindrical pile and displacements measured by two magneto-strictive linear position transducers. The data were collected with a sampling rate of 2000 Hz. Eight different constant carriage speeds have been compared, where the carriage speed is interpreted as the ice drift speed. The four lowest carriage speeds were tested for 300 s, the four highest carriage speeds were tested for 200 s. We increased the test time for low ice drift speeds to allow for the removal of transient effects resulting from the first impact with the ice while still having sufficient data to analyse. For some ice drift speeds, tests had been captured in two test IDs. Data from those test IDs have been merged in the present study. Merged time series are indicated in the figures accordingly. Data shown the present study, when not indicated otherwise, concern the last 175 s of each test. Maximum values are calculated as the 99th percentile of the data, the minimum as the first percentile. Full time series analysed can be found in the supplementary material.

3. Effect of wind-ice misalignment on the development of ice-induced vibrations

Statistics of resultant global ice load ($F_{res} = \sqrt{F_{x_p}^2 + F_{y_p}^2}$) and resultant structural displacement ($d_{res} = \sqrt{d_{x_p}^2 + d_{y_p}^2}$) of a 0°-, 30°- and 90°-misaligned scenario (further: 0°, 30° and 90° scenario) are shown in Fig. 5. Maximum, mean and standard deviation are shown for eight tested ice drift speeds in a 0° and 90° scenario and for four tested ice drift speeds in a 30° scenario.

Focusing on the ice load first, the highest maximum resultant ice load develops for the lowest ice drift speed tested (here: 5 mm s^{-1}), independent of the misalignment angle. The highest maximum load over all

misalignment angles can be found for the largest misalignment angle. The difference in the highest maximum ice load between an aligned and a misaligned scenario is larger than the difference between the highest maximum ice load of the two misaligned scenarios.

Differences in the resultant ice load between the 0° and 90° scenarios can be partly explained by the variation in ice thickness (shift of the mean ice load) during the experiments, but are also related to the different ice-structure interaction for the different misalignment angles as discussed in more detail below.

Overall, we recognise a decreasing trend of all statistics over all scenarios from low ice drift speeds to higher ice drift speeds. However, three exceptions can be observed. The first exception, observable in the 30° and 90° scenario, occurs for an ice drift speed of 10 mm s^{-1} as we observe a drop in the ice load statistical measures here. The second exception occurs for the highest ice drift speed tested (here: 50 mm s^{-1}) in the 0° and 90° scenario. We notice an increase of the statistical measures. The third exception is that the mean ice loads for 90° scenarios are rather constant for intermediate ice drift speeds.

Analysing statistical measures of the structural displacement, the largest maximum structural displacement per misalignment angle occurs for the lowest ice drift speed tested (here: 5 mm s^{-1}) in the 0° and 30° scenario, while it occurs for an ice drift speed of 15 mm s^{-1} in the 90° scenario. This displacement is also the largest displacement of the three presented scenarios. The mean resultant displacements are largest for the lowest ice drift speed for all three scenarios. Differences of mean displacements and standard deviations between the three scenarios are smaller in comparison to differences in the maximum displacement. A decreasing trend of all statistical measures in 0° and 30° scenarios was found from low ice drift speeds to higher ice drift speeds, while the trend levels off for higher ice drift speeds. As a main exception, the 90° scenario shows an increased magnitude in all statistics at ice drift speeds of 15 mm s^{-1} and 20 mm s^{-1}. At an ice drift speed of 50 mm s^{-1}, an increase of maximum structural displacements for the 0° and the 90° scenario are observable. Data points for the 30° scenario at an ice drift speed of 15 mm s^{-1} are labelled as outliers because the malfunction of one of the water spray nozzles created an artificially large ice thickness, which influenced the development of ice-induced vibrations significantly (see Section 5).

The identified differences in the trends for the statistical measures between the three scenarios are investigated by analysing the specific
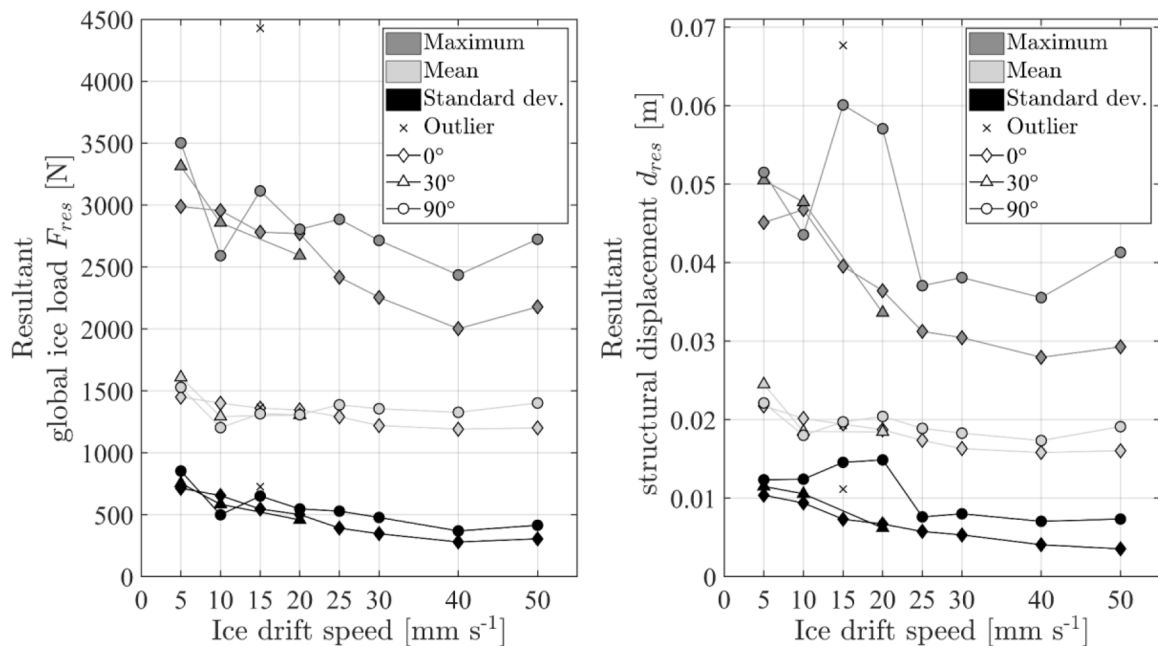

Fig. 5. Statistics of resultant ice loads (left) and resultant structural displacements (right) for three different misalignment scenarios.

time series.

First, we consider the ice load decrease in the 90° scenario for an ice drift speed of 10 mm s^{-1}. The time series of resultant global ice load and structural displacement for that ice drift speed are shown in Fig. 6. The figure shows that large-amplitude multi-modal vibrations occur for all misalignment angles tested, but a steady-state load and response is only obtained in the 90° scenario. One might explain the difference in the steadiness of the interaction by a lower damping in the direction of ice loading in the 90° scenario.

Peak loads in the 0° and 30° scenarios are larger than in the 90° scenario at an ice drift speed of 10 mm s^{-1}, which seems to be related to short instances of intermittent crushing, characterized by a saw-tooth load and response pattern with a period longer than the first natural period. Intermittent crushing resulted in larger peak loads compared to peaks from the multi-modal interaction in the 90° scenario (Fig. 6). It is possible that the variation in ice properties, such as thickness and strength, plays a role here. Thicker and stronger ice would result in a change in the interaction which may cause a shift to a different regime of ice-induced vibrations. However, as the ice thickness in the 0° and 30° scenarios was slightly smaller than that during the 90° scenario, we consider this explanation unlikely. Another explanation is that the structural motion due to the predefined wind force interferes with the synchronisation between ice and structure and therefore inhibits the development of the ice-induced vibration regime. This explanation is further investigated in Section 4.

The 90° scenario resulted in large displacements for ice drift speeds of 15 mm s^{-1} and 20 mm s^{-1} for which time series of the latter are shown in Fig. 7. The comparison reveals that the 90° scenario results in multi-modal interaction with a strong amplified first-global-bending-mode response, whereas the 0° and 30° scenarios result in short periods of frequency lock-in in the second and third global bending mode. This result can be explained by the difference in the aerodynamic damping, which dampens the first mode oscillations significantly for the 0° and 30° scenarios where the ice is more aligned with the wind.

The effect of higher aerodynamic damping in the 0° scenario compared to the 90° scenario can further be seen for the ice drift speed of 50 mm s^{-1} (Fig. 8), where frequency lock-in in the second global bending mode still develops for short periods of time at this high speed in the 90° scenario while in the 0° scenario only continuous brittle crushing is observed. For the 0° scenario we observe a peak in the brittle crushing load around 860 s, which is related to the artificially high ice thickness created by the malfunction of one of the water spray nozzles as discussed in Section 6.5.

To summarize, the differences in vibrations between the three different scenarios seem to be mainly caused by the lower total damping in ice load direction when misalignment between wind and ice direction

was tested, with some effect of variation in ice properties always present. For the 90° scenario, sustained vibrations are more likely to develop, and the regimes of ice-induced vibrations develop up to higher ice drift speeds. This is a common observation for structures with low damping interacting with ice.

4. Effect of structural motions due to applied wind loading on the ice-structure interaction

In this section, we investigate if the response of the structure to the predefined wind load can interfere with the quasi-static load build-up process in the ice, thereby reducing the ice-load level and maximum structural displacements of aligned or slightly misaligned scenarios, when compared to highly misaligned scenarios for the lowest ice drift speed (Fig. 5 at 5 mm s^{-1}).

To investigate the effect, we compare time series and corresponding amplitude spectral densities between a 0°, idling scenario and a 0°, operational scenario for intermittent crushing (here at 5 mm s^{-1}) in Fig. 9. The ice load time series of the operational scenario shows lower ice load peaks and a difference in the amplitude spectral density of the ice load compared to that of the idling scenario. The spectrum of the ice load for the idling scenario shows content for low frequencies (quasi-static) and frequencies slightly above the first eigenfrequency. Note that the first two structural eigenfrequencies are indicated with green vertical lines. The spectrum of the operational scenario shows several peaks and a smaller contribution of lower natural frequencies when compared to that of the idling scenario. Analysing the applied wind load fluctuation in the frequency domain, we notice that the frequencies present here are also present in the amplitude spectral density of the ice load for the operational scenario (e.g. 0.09 and 0.25 Hz, which are highlighted by dashed, black vertical lines). This is an indication that the structural vibrations due to the applied wind load are present at the ice action point. As the ice-structure interaction is highly sensitive to the relative velocity between ice and structure, higher mode vibrations will have an effect during the load build-up phase. Further testing would be required to confirm that indeed in all cases the peak loads for aligned, idling scenarios are higher than in aligned, operational scenarios, though the explanation in terms of higher mode vibrations changing the relative velocity during interaction, provoking a premature global ice load failure, seems plausible.

This effect would also allow to explain why aligned or slightly misaligned scenarios fail to result in steady-state ice-induced vibrations as shown in Fig. 6. However, because the aerodynamic damping was present in the ice drift direction and influenced the vibrations, we cannot provide a general conclusion for all types of ice-induced vibrations.

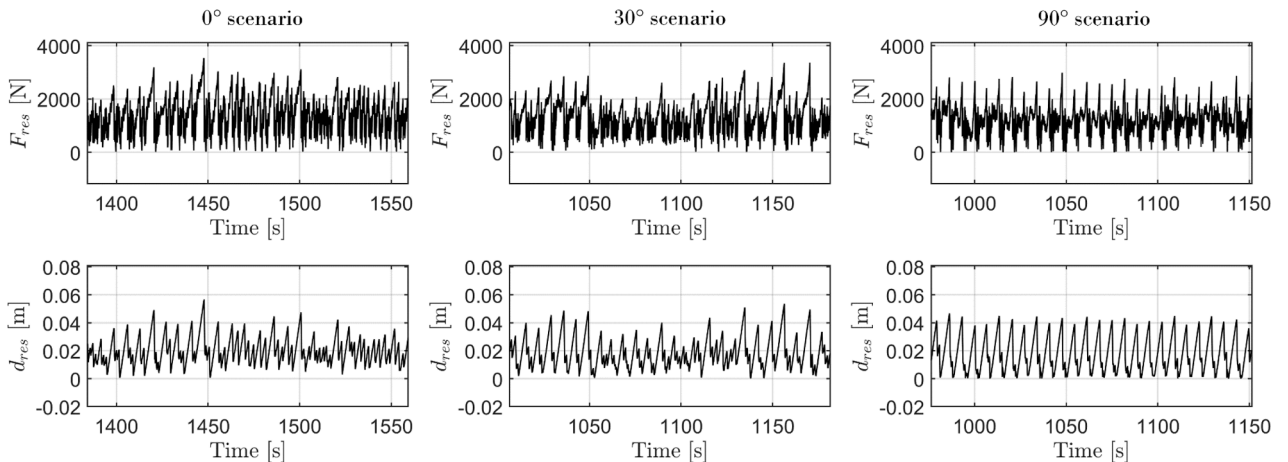The results presented in Section 3 do not allow to identify to what

Fig. 6. Time series of resultant global ice load and structural displacement for a 0°, 30° and 90° scenario for an ice drift speed of 10 mm s^{-1}.
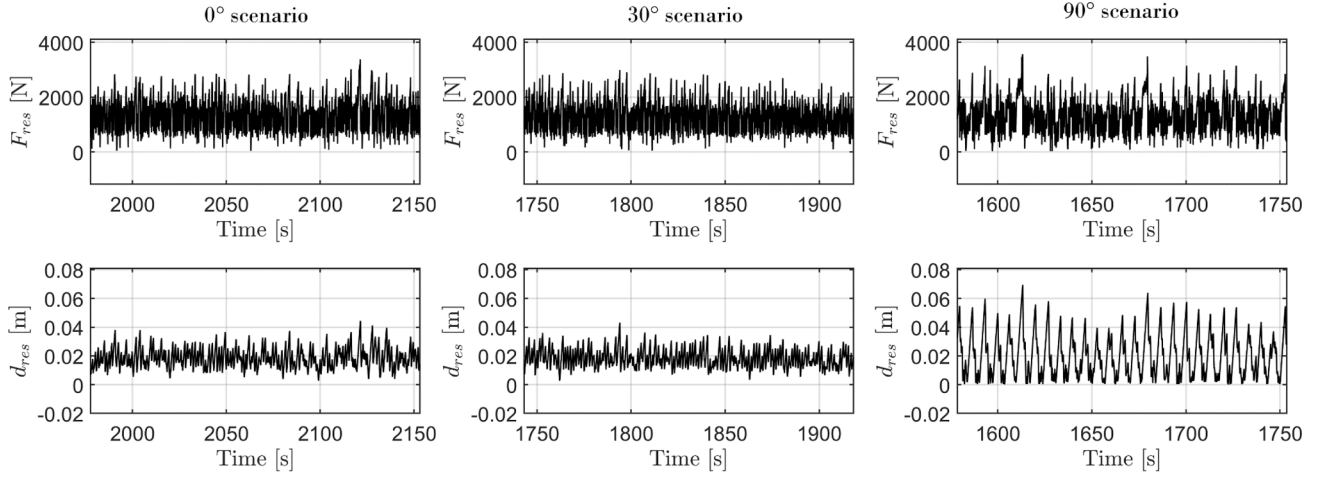
Fig. 7. Time series of resultant global ice load and structural displacement for a 0°, 30° and 90° scenario for an ice drift speed of 20 mm s^{-1}.
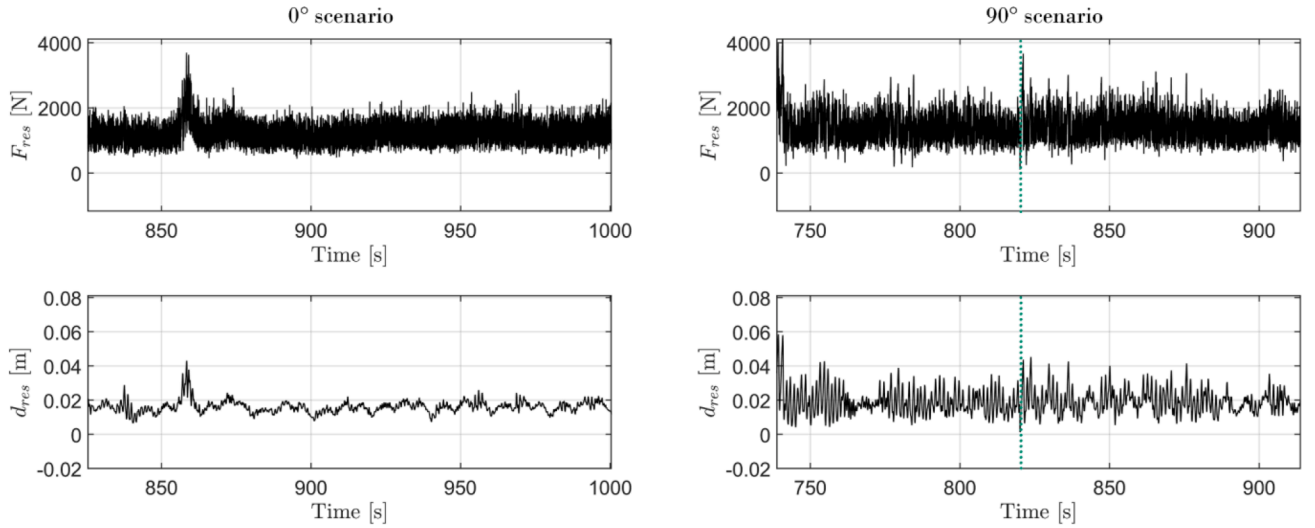

Fig. 8. Time series of resultant global ice load and structural displacement for a 0° and 90° scenario for an ice drift speed of 50 mm s^{-1}. The green light line indicates where two test IDs have been merged.

extent the additional wind-induced displacement in crosswise direction influences the development of ice-induced vibrations yet. In the next section, we therefore investigate if the wind-induced motions cause crushing of the ice perpendicular to the ice drift direction in a mis-aligned scenario, thereby potentially influencing the global ice load, structural response, or spatial distribution of the ice load.

5. Effect of crosswise wind-induced structural motions on the ice

When the ice drift and wind direction are misaligned by 90°, wind-induced displacements at the ice-action point, when inducing large enough loads, could theoretically cause crushing of the ice at the sides of the structure. To investigate if the ice in lateral direction is indeed crushed, we compare test results of a 90° scenario to an aligned (0°), idling baseline scenario.

5.1. Ice load and structural displacement in x_p- and y_p-directions

First, the statistics of the ice loads in x_p- and y_p-directions are compared in Fig. 10. The resultant load on the structure is, for a large part, defined by the load in the ice drift direction (y_p) as the different

scale of the y-axes shows. The wind-induced displacements in the 90° scenario cause lower minima and higher maxima in the ice loads perpendicular to the ice drift direction (x_p) at low ice drift speeds. The opposite is true for the loads in the ice drift direction (y_p). For higher ice drift speeds, the effect of the wind seems negligible from the statistical measures.

Second, the statistics of the structural displacements in x_p- and y_p-directions are compared in Fig. 11. The maximum and minimum of wind-induced displacement at the ice action point in the absence of ice are shown in the plot for x_p by dashed lines. Comparing the maximum and minimum displacements in the 90° scenario to those in the absence of ice shows that the measured displacements do not reach the numerical open-water amplitude for low ice drift speeds. The ice is clearly constraining the structural motion in x_p-direction. At higher ice drift speeds, this constraining effect seems to be less than at lower speeds, which could relate to the fast repetitive failure of the ice at high ice drift speed allowing the structure to move around more easily in the clearing created in the ice. The statistical measures of displacements in y_p-direction do not show any remarkable difference between the idling and the 90° misaligned scenario, in the same manner as for the loads in Fig. 10.

Fig. 12 shows time series of structural displacement in x_p- and
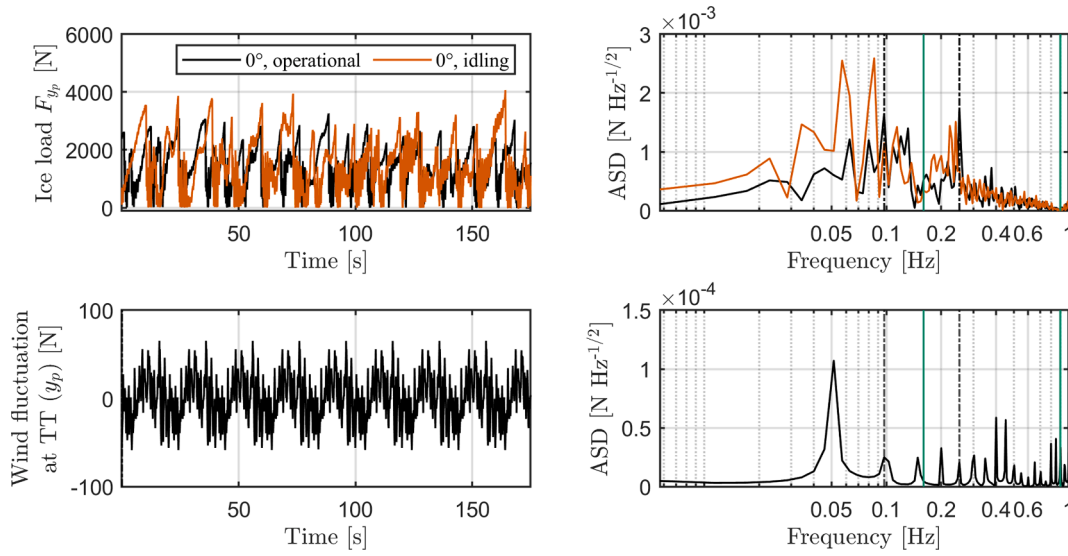
Fig. 9. Ice load and wind fluctuation time series and corresponding amplitude spectral densities of 0°, idling and 0°, operational scenarios. The first and second natural frequencies are indicated by vertical green lines. (For interpretation of the references to colour in this figure legend, the reader is referred to the web version of this article.)
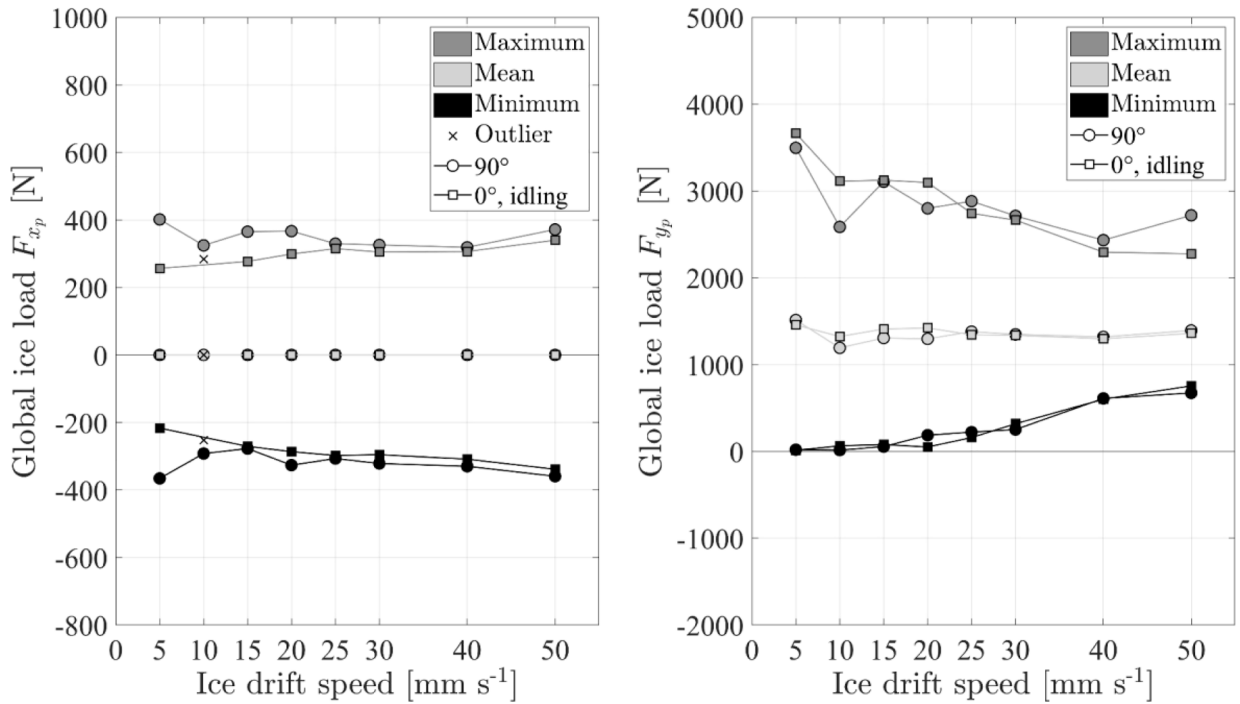

Fig. 10. Statistics of global ice loads in x_p- and y_p-directions for a 90° misaligned and an aligned, idling scenario.

y_p-directions, as well as the numerical wind-induced displacement at the ice action point in x_p-direction in the absence of ice for an aligned, idling scenario at an ice drift speed of 5 mm s^{-1}. Note that the two y-axes have a factor ten difference in their limits. A case of intermittent crushing is found for this speed during which the motions of the structure in x_p-direction occur mainly after moments of global ice failure and into different directions quasi-randomly. As this observation is interpreted as such that the structure is moving into the space created at the moment the ice fails, it is shown that cascading (non-simultaneous) failure (not purely instantaneous, simultaneous failure) takes place across the circumference of the pile.

The same plot for a 90° scenario at the same ice drift speed in Fig. 13 (top) shows that the structure is following the wind-induced

displacement immediately after global ice failure (e.g. at t = 720 s). During the load build-up phases, we see that the structure is moving due to the wind load, but its motion at the ice action point is clearly constrained by the ice (e.g. 750 s – 760 s). For a high ice drift speed (40 mm s^{-1}) as shown in Fig. 13 (bottom), the motion in x_p-direction starts to approach the wind-induced displacements for an ice-free scenario. This can be explained by the events of ice failure following one another more rapidly at this speed (i.e. reduced contact area and confinement by the ice), creating the space for the structure to move.

Finally, we want to draw the attention to the effect of small(er) misalignment angles (here φ = 30°) on the development of ice-induced vibrations in the direction perpendicular to the wind (see Fig. 4). In the 30° scenario, the ice, now crushing slightly misaligned against the
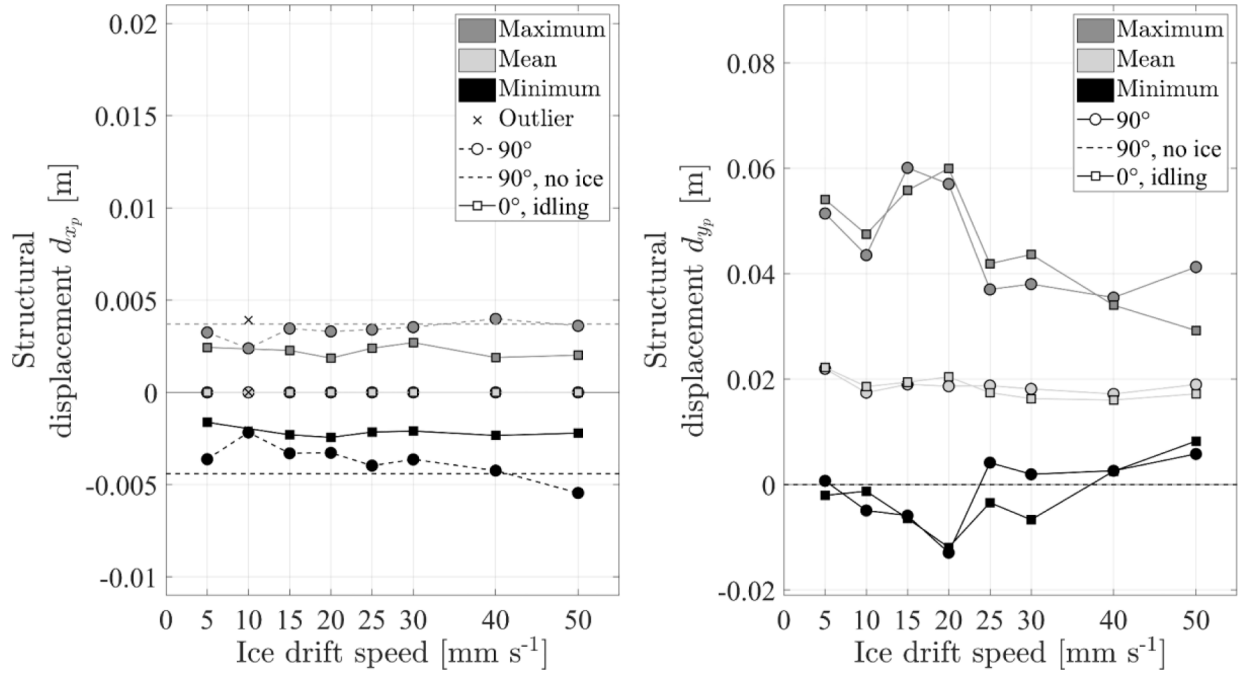
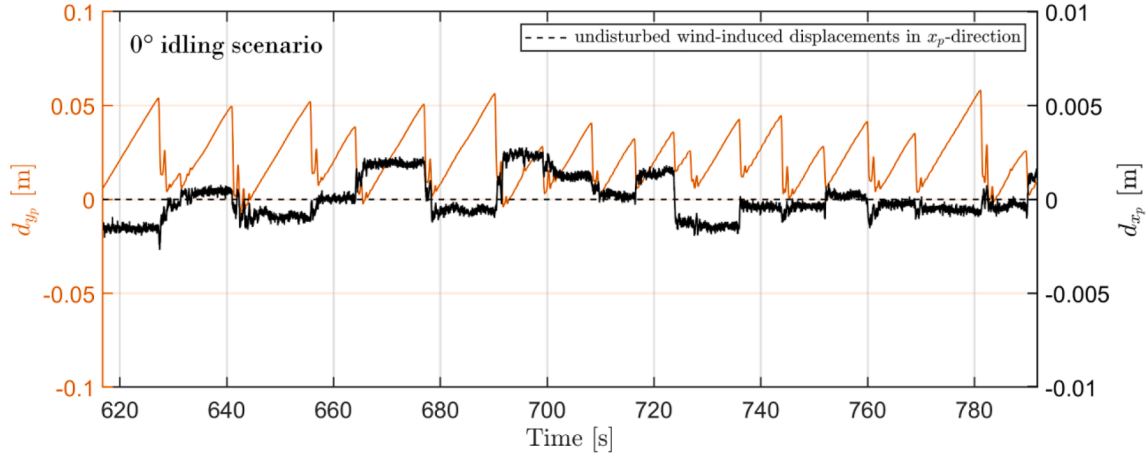**Fig. 11.** Statistics of displacements in x_p- and y_p-directions.

Fig. 12. Time series of structural displacement in x_p- and y_p-directions for an ice drift speed of 5 mm s^{-1} for an aligned, idling scenario (Test ID 590).

structure, causes a loading of the structure in x_s- and y_s-directions, as can be seen in Fig. 14. As the aerodynamic damping is added to the structural damping in wind-direction (here: y_s), structural vibrations in x_s-direction are consequently less damped.

The effect of the low damping on the structural vibrations on the projected x_p-direction can be observed in Fig. 15 as vibrations of higher frequency occur once the structure snaps forward after a global ice failure event. However, it is striking that the structure vibrates with a low amplitude (~0.5 mm) while still being constrained by the ice. Fig. 16 reveals that the frequency of the low amplitude vibration ($\approx$1.1 Hz) is higher than the second eigenfrequency and lower than the third eigenfrequency of the implemented structure. Thus, we surmise that the intact ice is in contact with the structure and does not break for low amplitude forcing and high frequency, but rather causes an added stiffness effect from the perspective of the structure. This example shows that relatively small misalignment angles between ice and structure can lead to vibrations of small amplitude and high frequency in the direction perpendicular to the wind.

In summary, it is found that the ice provides a confining effect for low

relative velocities between ice and structure in a misaligned load scenario. For high relative velocity, the confining effect is less which is attributed to the larger number of failure events in the ice, creating the space for the structure to move. Additionally, for the 30° scenario, vibrations of relatively high frequency and low amplitude develop in the direction perpendicular to the wind. For those vibrations, the ice does not seem to break when interacting with the structure but instead cause an added stiffness effect. Added stiffness here means that the structure is experiencing a constant constraining by the ice in lateral direction. The frequency observed is that of the combined ice-structure system.

It is uncertain if the clearing of ice at the structural sides is caused by wind-induced motion or by the ice-induced motion solely. To address this question, the spatial distribution of the ice loads around the circumference of the structure is analysed next.

5.2. Spatial distribution of the ice load

Normalized probability distributions of the resultant ice loading direction across the pile circumference are shown for the eight tested ice
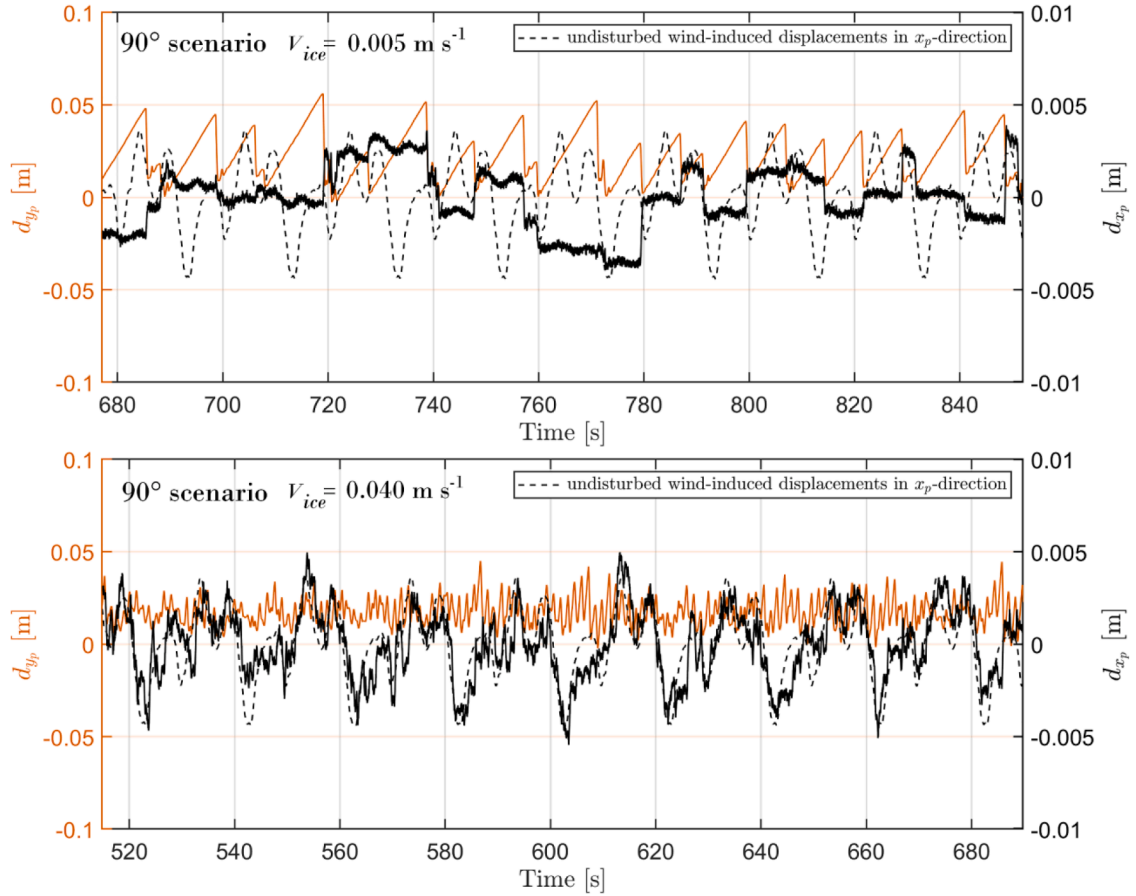
Fig. 13. Time series of structural displacement in x_p- and y_p-directions for an ice drift speed of 5 mm s^{-1} (top) and 40 mm s^{-1} (bottom) for a 90° scenario (Test ID 387 and 407).
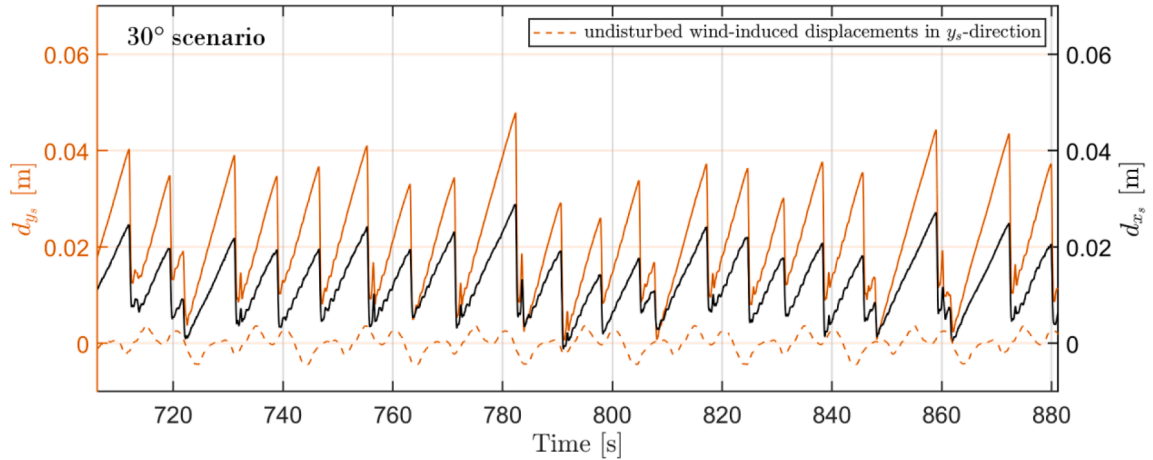

Fig. 14. Time series of structural displacements in the turbine coordinate system for a small misalignment angle (Test ID 392).

drift speeds for the 90° scenario and the aligned, (0°) idling scenario in Fig. 17. For normalization, the number of elements per bin c_i have been divided by the number of elements for the chosen input data N. For quantification of differences, three intervals along the structural surface (I = [340° to 358°], II = [359° to 1°], III = [2° to 20°]) have been defined. For each interval, the cumulative probability is given in percentages.

The normalized probability distributions of the resultant ice loading direction reveal that the structure, independent of the misalignment angle and ice drift speed, is mostly loaded in the direction of the ice drift.

Values associated with interval II decrease for the 0°, idling scenario from lower to higher ice drift speeds (33% to 21%). Instead of being loaded in the main ice-drift direction as for low ice drift speeds, the structure at high ice drift speeds is more likely to be loaded in interval I and III as here values increase from 26% (I) and 28% (III) to 39% for both. This shift of values relates to the change in ice-structure interaction from intermittent crushing to continuous brittle crushing where for the former, long load build-up phases are associated with loading in the direction of ice drift. Further note that the structure at low ice drift speeds shows an increased normalized probability distribution of the
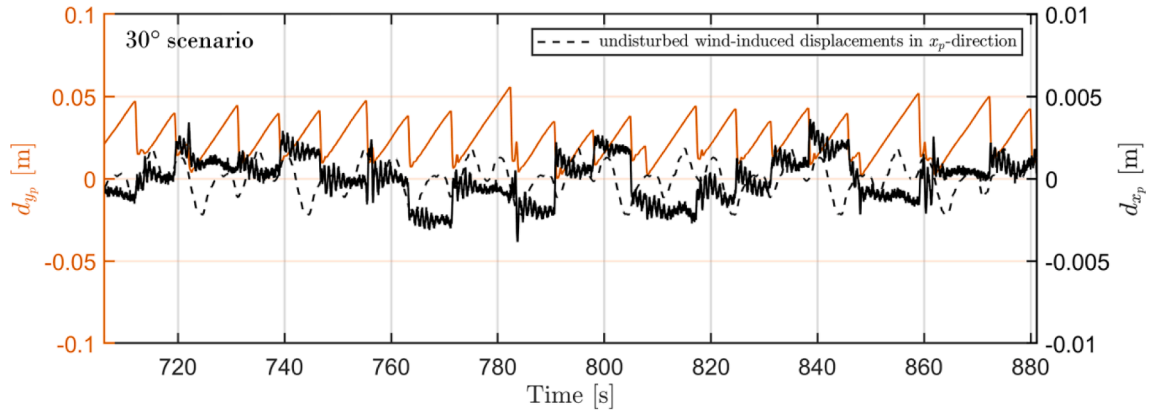
Fig. 15. Time series of structural displacements in the pile coordinate system for a small misalignment angle (Test ID 392).
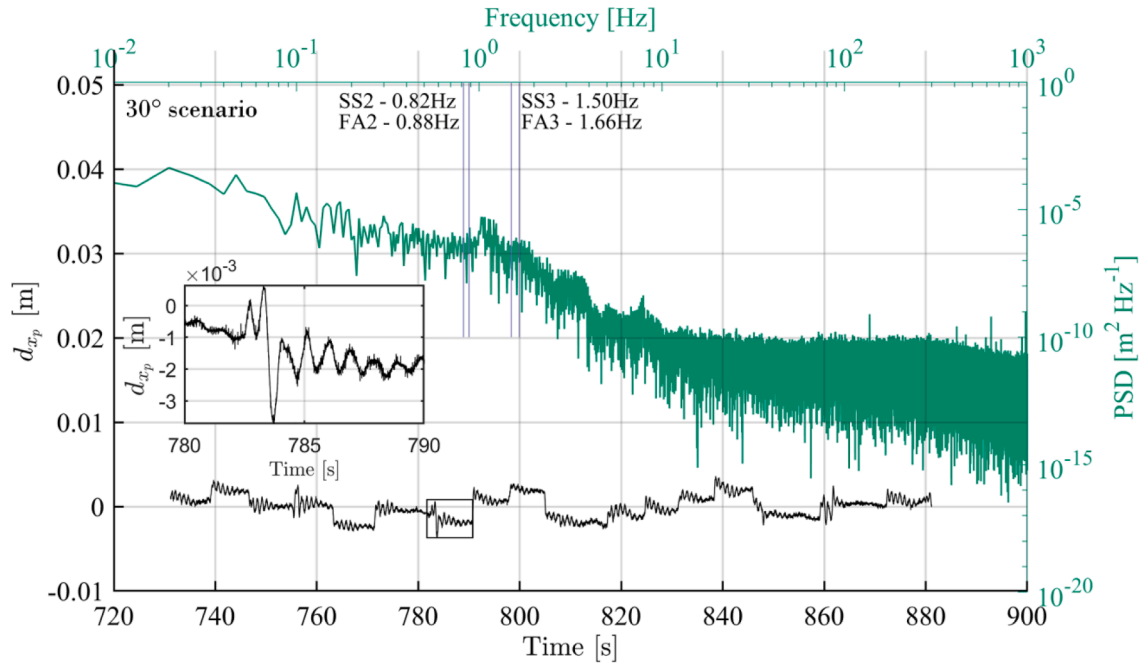

Fig. 16. Power spectral density and time series of the structural displacement in x_p-direction indicating the natural frequencies (Test ID 392).

resultant ice loading direction outside of the defined intervals. The reason here is the added lateral confinement of the ice, increasing the probability of loading at the structural sides (see Fig. 10-left).

The effect of a wind-ice misalignment on the normalized probability distributions of the resultant ice loading direction is largest for low ice drift speeds (5 mm s^{-1} – 20 mm s^{-1}). Once the wind is acting on the turbine, the structure is loaded in interval I and III more frequently when compared to the 0°, idling scenario. The normalized probability distributions become left-skewed as the mean load of the applied wind fluctuation is positive, thereby causing a positive offset into the direction of wind load application.

For the highest ice drift speed, the occurrence probabilities of the aligned and misaligned scenario are almost fully overlapping. The wind-caused displacement in x_p-direction does not seem to have any effect on the resultant ice load direction. From this we conclude that the wind-induced motions do not crush the ice at the sides of the structure to any significant extent, which would have otherwise resulted in a different distribution of the normalized probability of the resultant ice load when compared to an idling scenario.

6. Discussion

First, we discuss main results in the context of the aim of the study: to investigate the effect of wind-ice misalignment on the development of ice-induced vibrations. After that, we discuss the generalisation of the results and reliability of the test data.

6.1. Effects of wind-ice misalignment on the development of ice-induced vibrations

The results shown in Section 3 align with the general understanding of ice-induced vibrations that lower damping leads to high-amplitude structural vibrations. In the case of an offshore wind turbine, wind adds aerodynamic damping to the system. As the wind is primarily acting at the top of the structure, vibrations related to modes with a high mode-shape amplitude at the tower top (e.g. first eigenmode) are more significantly damped during the ice-structure interaction. This explains the findings in Figs. 5 and 6, as ice-induced vibration regimes related to first-mode vibrations (90°, 15 mm s^{-1} and 20 mm s^{-1}) start to appear with an increase in the misalignment angle. However, the aerodynamic damping cannot explain the observed increase of maximum ice loads
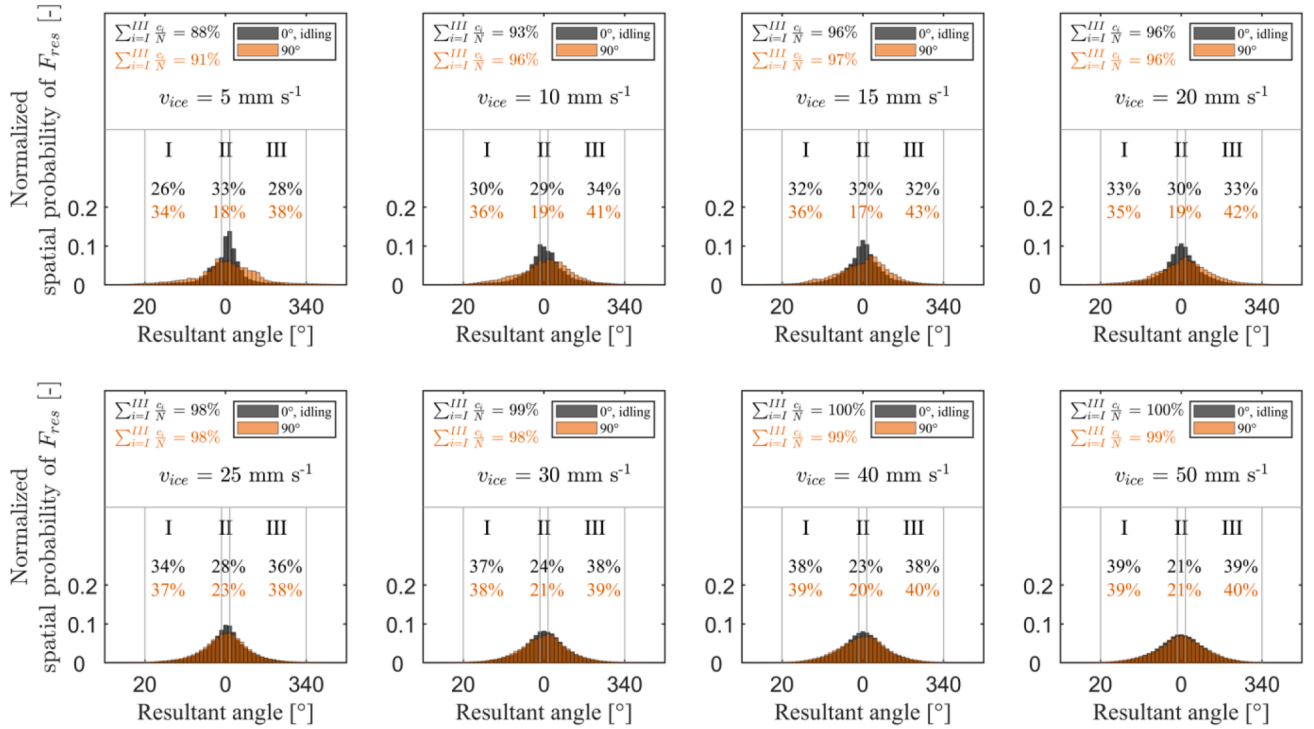
Fig. 17. Normalized resultant ice load probabilities over the resultant direction angle.

during intermittent crushing (5 mm s^{-1}) when the misalignment angle increases (see Fig. 5). We think that the increase in ice load with increasing misalignment angle during intermittent crushing is instead related to the absence of wind-induced structural displacements interfering with the interaction between ice and structure as explored in Section 4. It is unknown to what extent this interference would remain when the full interaction between wind and RNA is included in an experiment.

6.2. Sensitivity of results to local changes in ice properties and equipment malfunction

We attempted to keep the properties of the ice constant during the campaign and change only the wind-ice misalignment angle. However, it is possible that slight differences in (ice) temperature could have

affected the development of ice-induced vibrations. One example of the influence of a substantial change in (ice) temperature on the development of ice-induced vibrations during this campaign is discussed by Hendrikse et al. [44], showing the importance of temperature in general. Large differences in the ice thickness could also significantly influence the development of ice-induced vibrations. According to Table 3, differences in the measured ice thickness were relatively large ($\sigma = 3.4$ mm). The measurement of the ice thickness was challenging as additional ice growth under the sprayed ice thickness occurred during the day which had to be manually removed during the measurement, thereby introducing an error and deviation in the measurements.

A significant local ice thickness variation (ice inclusion) can influence the development of ice-induced vibrations. The outlier, identified for the 30° scenario at an ice drift speed of 15 mm s^{-1} (see Fig. 5), is caused by a sudden change in ice thickness. A defect in a water spray
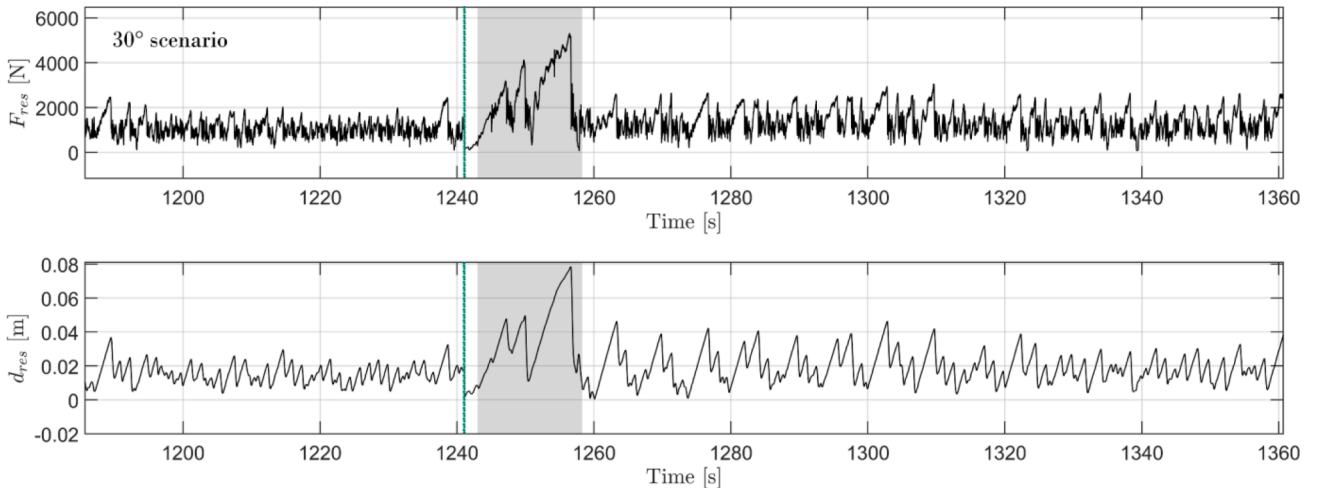

Fig. 18. An artificially high ice thickness (shaded in grey) introduced a new phase of transient ice-induced vibrations (Test ID 394). The green line indicates where two tests have been merged. (For interpretation of the references to colour in this figure legend, the reader is referred to the web version of this article.)

nozzle resulted in a linear band of stronger ice as can been seen in Fig. 7 from [39]. While the ice thickness change has a limited effect on the brittle crushing load (quasi-static response in Fig. 8), time series for lower ice drift speeds (dynamic response) show that the increased thickness introduces a phase of transient ice-induced vibrations which eventually disappear again after about 100 s (see Fig. 18). The ice inclusion coincidently occurred after an interruption of the test measurement (at the green dotted line).

Another example of an outlier can be seen for the 0°, idling scenario at an ice drift speed of 10 mm s^{-1} in Fig. 19. The reason for the increased structural displacement is that the electrical actuator in x_p-direction stopped working during testing. A larger load drop occurred once we restarted the test at t = 925 s, as the ice already had been damaged, thereby providing an artificially high contact area as it was smoothened by previous contact with the structure. The outlier is marked as such in Fig. 10-left.

Showing these two exemplary events, we want to emphasize that maximum ice loads should be considered with care. To minimize the effect of local fluctuations in ice thickness and ice strength on the statistics, we used 99% and 1% quantiles as maximum and minimum in the present study. Statistics were based on the last 175 s of a time series to minimize the effect of initial vibrations on the statistics measured. However, ice crushing tests are limited by the available length of ice, which is why initial vibrations with low frequency are still observable in some time series (e.g. see Fig. 8).

6.3. Ice deformation and crushing at the side of the structure

It was shown that the ice is confining the structure for low relative velocity (see Figs. 12 and 13). Once the relative velocity between the structure and the ice increases (e.g., at an unloading phase during intermittent crushing or during continuous brittle crushing), confinement reduces (see Fig. 13). Structural displacements in x_p-direction at low ice drift speeds (see Figs. 12, 13-top, and 15) showed that the structure moves out of the main ice-drift direction once it snaps forward after a global ice failure. The direction of deviation seems random. We have seen that the measured displacement in x_p-direction does not match exactly the expected open-water wind-induced displacement at high relative ice drift speed (see Fig. 13 - bottom). At some instances, the structure is still confined, while at other instances the measured displacement exceeds the open-water wind-induced displacement (see Fig. 13-bottom, t = 605 s). We speculate that the latter events are caused by the superposition of responses caused by wind and ice.

Analysis of structural responses in x_p-direction revealed that a misalignment angle between 0° and 90° leads to high frequency and low amplitude vibration in the cross-direction (see Figs. 15 and 16). As those vibrations did not match one of the natural frequencies of the implemented structure, it is reasonable to assume ice-structure coupling.

We suggested that the structure at high relative velocities crushes the ice at the structural side, providing conditions allowing the open-water wind-induced motion to develop. In Fig. 17, we showed that the spatial probability of the resultant ice load of the 0°, idling scenario is nearly the same as for the 90° scenario. However, loading does not necessarily reveal information about the failure of ice. Nevertheless, the ice does constrain the wind-induced motion for low ice drift speeds (see Fig. 11). Thus, wind-induced motions do not manage to crush ice at the structure side for these ice drift speeds. As the wind-induced motion does not change for higher ice drift speeds, the phenomenon of ice crushing at the structure side is caused by the non-simultaneous ice failure across the circumference of the pile, not by the wind. In addition, it could be argued that the overall stress level of the wind-induced displacements is ultimately too low to crush the ice.

6.4. Generalisation of results

Based on the results of the experiments for existing structures where full-scale data are available [44], we are confident that the results of these tests are qualitatively representative for a full-scale event of ice-induced vibrations of an offshore wind turbine.

In the present study, a lumped mass model of a 14 MW offshore wind turbine was used, instead of a full offshore wind turbine in a fully-coupled aeroelastic solver. A full aeroelastic code and structural model, including blades, could be theoretically implemented in a microcontroller and may be considered in future experiments. This method could be used to investigate if the effect of wind interference on the development of ice-induced vibrations still takes place when the full RNA is accounted for.

During our test campaign we focussed our analysis on one wind speed and, respectively, on one set of linearized wind load fluctuations and aerodynamic damping at rated wind speed. Wind sets with smaller aerodynamic damping are expected to result in smaller differences between a misaligned and aligned load scenario, and higher vibrations for an aligned case. Wind sets with higher aerodynamic damping are expected to result in larger differences between a misaligned and aligned load scenario, and lower vibrations for an aligned case. A minor amplitude change of the wind-induced displacement at the ice action point is not likely to have any effect on the development of ice-induced vibrations.

A static wind load at tower top, thus a wind-induced mean offset at waterline, was neglected as it was not expected to have a significant
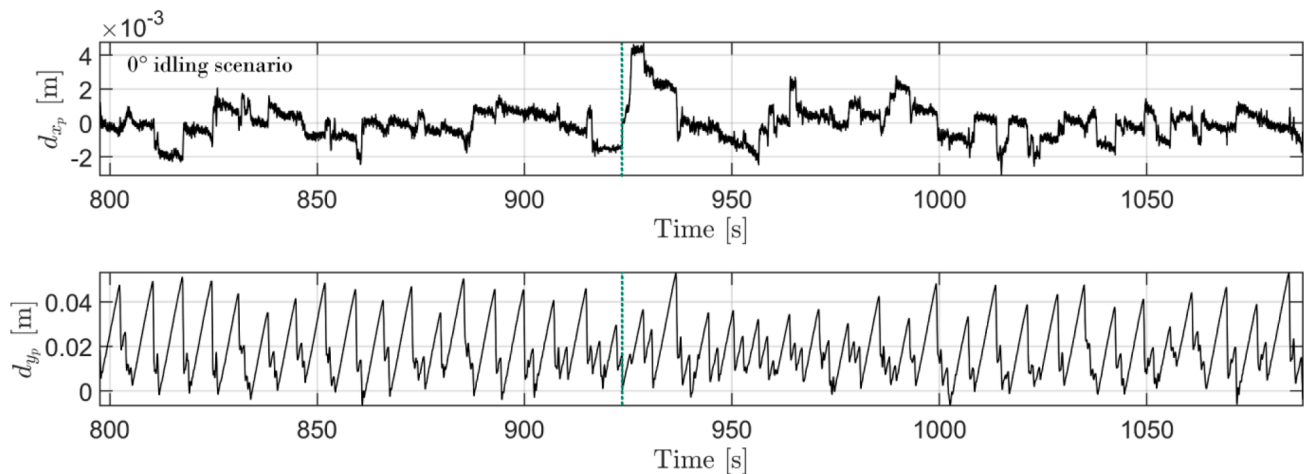

Fig. 19. Smoothened ice due to a system stop introduces a locally increased structural displacement once resumed (Test ID 591). Here the green line indicates where two tests have been merged and consequently where the test resumed.

influence on the development of ice-induced vibrations. For the overall analysis of a support structure of an offshore wind turbine, and the relative importance of the different alignment scenarios for design, it is important to consider this load contribution as well.

6.5. Data reliability

While post-processing the raw data, we noticed that ice was 'crawling up' the pile during experiments. Once the ice came close to one of the strain gauge rings and caused temperature-induced strain, an artificial bending stress was included in the measurement. Our tested pile was sensitive to those stresses as aluminium provides a high thermal conductivity and the strain gauge bridge in the inside of the pile was relatively large.

A photograph of the pile and corresponding load data of an 'ice crawling' event are shown in Fig. 20. The ice pieces close to the strain gauge ring shift the identified load direction by about 20° for the ring closest to the ice (Ring 2) and by about 12° for the ring with maximum distance to the ice (Ring 1). The load cells attached to the actuators show that the true loading direction had no such offset. We were able to quantify the offset error in the strain gauge measurements by comparing the medians between the strain gauge and load cell measurements. We compared the median because the load cells measure additional inertial loading (higher peaks). The median is not as sensitive to increased peak measurements as a mean value would be. The calculated difference was subtracted for both x_p- and y_p-directional loads in the present study. We observed that the error due to 'crawling' ice in y_p-direction was small compared to the error in x_p-direction. Using the determined load offset,
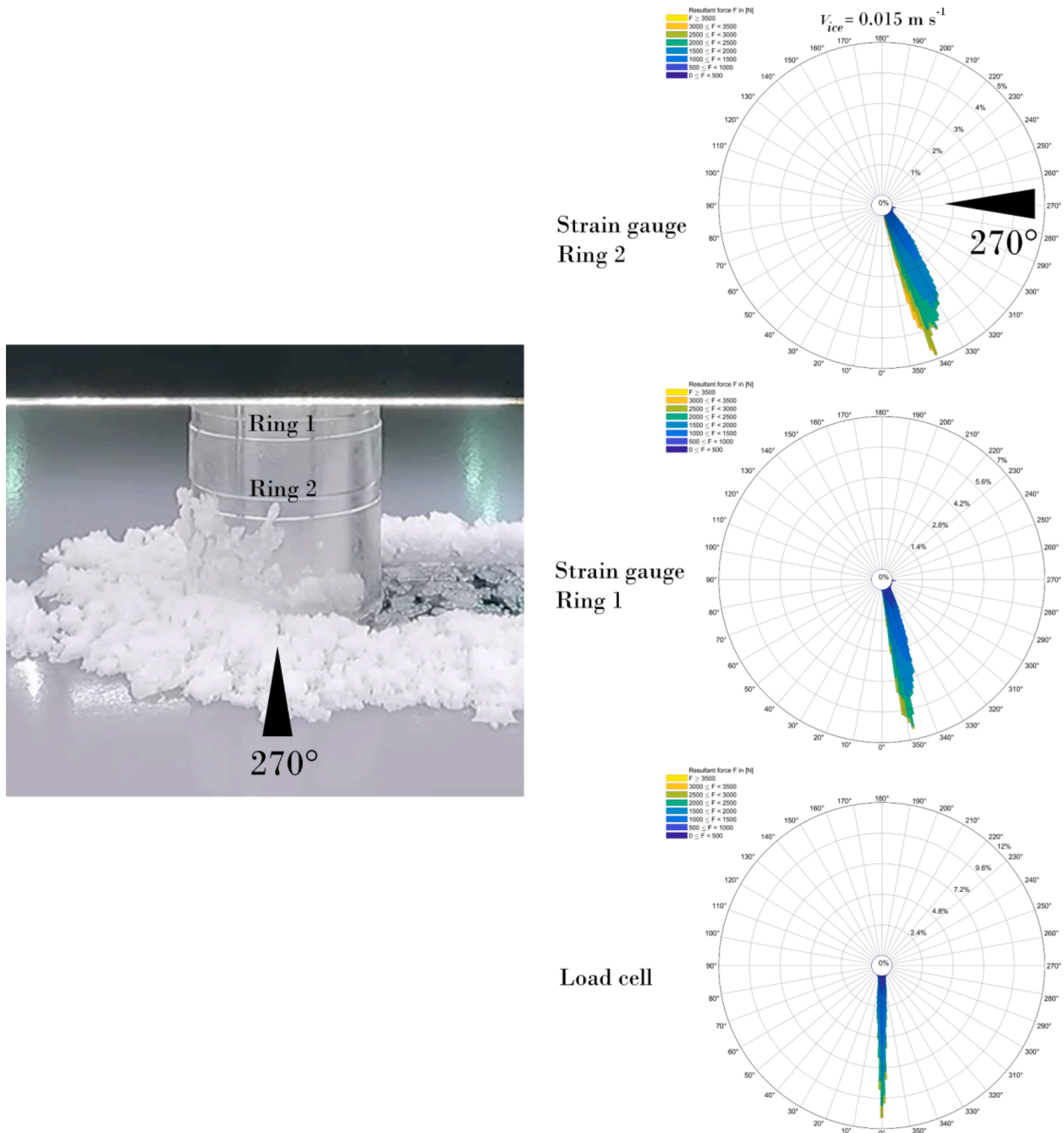

Fig. 20. Ice attached to the pile influenced the strain gauge measurements. The data shown here are based on the last 100 s of data of test ID 384 and are based on the wind rose tool from [48].

we calculated and applied the corresponding offset for the structural displacement using the numerical structural model. As the ice was 'crawling' during a single test, thereby slightly changing the temperature-induced bending stress amplitude over time, we further applied a linear detrend function (MATLAB R2021a) on the data in x_p-direction.

As the compensation for the crawling was not solved during the test campaign, but only during the post-processing, it is undeniable that our hybrid test method is influenced by this error. In general, we do not think that this error significantly influences our results, as we would have, in any case, overestimated the load in x_p-direction, but still do not see any significant influence of the crushing on the vibration pattern.

The statistical value of our data can be questioned as we did not repeat test runs due to limited test length. Instead of repetition, we decided to increase the test duration of single tests, allowing to use only the last 175 s of a single test which was more likely to be representative of a steady-state structural response. The full time series of the measurements can be found in the supplementary material, indicating the data used in the analysis.

7. Conclusion

An experimental study was conducted to investigate the effect of wind-ice misalignment on the development of ice-induced vibrations of offshore wind turbines. Experiments were based on a real-time hybrid test method implementing a linearized modal lumped mass representation of an offshore wind turbine. The structural model excluded blade interaction but included virtual wind loading and aerodynamic damping. The results demonstrate that, in a misaligned scenario, steady-state high-amplitude ice-induced vibrations could develop more easily when compared to an aligned scenario. This can be explained by the absence of aerodynamic damping in the direction of ice drift and ice loading. The wind-induced displacements at the ice-action point do not seem to have a significant effect on the development of ice-induced vibrations in a misaligned scenario, though there are indications these can disturb the interaction process in an aligned scenario as it was found that structural vibrations due to wind loading interfere with the development of a quasi-static load build-up in some tests. The ice was found to constrain the lateral structural motion for low ice drift speeds in a misaligned scenario, whereas for high ice drift speeds the open-water wind-induced displacement of the support structure is visible in the response of the structure. This is explained by the rapid succession of failure events in the ice (i.e. crushing of the ice edge) during continuous brittle crushing and clearing of the ice for the structure to move in cross ice-drift direction. A 30°-misaligned scenario resulted in lateral vibrations of the structure of relatively low amplitude and high frequency. For this scenario, the wind-induced motion was still constrained by the ice. The experimental results provide a basis for further study of the response of offshore wind turbines to misaligned wind and ice loading. The application of a fully-coupled aeroelastic software in combination with a full structural model of an offshore wind turbine in the microcontroller is recommended for further investigation of non-linear effects on the interaction between wind, blades, support structure, and ice.

CRediT authorship contribution statement

Tim C. Hammer: Conceptualization, Methodology, Validation, Software, Formal analysis, Investigation, Data curation, Writing – original draft, Visualization. **Hayo Hendrikse:** Conceptualization, Methodology, Investigation, Data curation, Resources, Writing – review & editing, Supervision, Project administration, Funding acquisition.

Declaration of Competing Interest

The authors declare that they have no known competing financial interests or personal relationships that could have appeared to influence the work reported in this paper.

Appendix A. Supplementary data

Supplementary data to this article can be found online at https://doi.org/10.1016/j.engstruct.2023.116106.

References

[1] Peyton HR. Sea ice forces. Proc. Conf. Ice Press. Against Struct. 1968:117–23. https://doi.org/10.4224/40001154.

[2] Blenkarn KA. Measurement and analysis of ice forces on cook inlet structures. Proc. Annu. Offshore Technol. Conf. 1970;II:365–78. https://doi.org/10.4043/1261-ms.

[3] Yue Q, Bi X. Ice-induced jacket structure vibrations in Bohai Sea. J Cold Reg Eng 2000;14:81–92. https://doi.org/10.1061/(ASCE)0887-381X(2000)14:2(81).

[4] Määttänen M. Experience of ice forces against a steel lighthouse mounted on the seabed and proposed construction refinements. In: Proc. 3rd Int. Conf. Port Ocean Eng. under Arct. Cond., Fairbanks, Alaska, USA: POAC; 1975. p. 857–69.

[5] Engelbrektson A. Dynamic ice loads on a lighthouse structure. In: Proc. 4th Int. Conf. Port Ocean Eng. under Arct. Cond., St. John's, Newfoundland, Canada: POAC; 1977. p. 654–63.

[6] Nordlund OP, Kärnä T, Järvinen E. Measurements of ice-induced vibrations of channel markers. In: Proc. 9th Int. Symp. Ice. Sapporo, Japan: IAHR, Vol. I; 1988. p. 537–48.

[7] Jefferies MG, Wright WH. Dynamic response of "Molikpaq" to ice-structure interaction. In: Proc. 7th Int. Conf. Offshore Mech. Arct. Eng. Houston, Texas, USA: OMAE, vol. IV; 1988. p. 201–20.

[8] Schwarz J, Jochmann P. Ice force measurements within the LOLEIF-project. In: Proc. 16th Int. Conf. Port Ocean Eng. under Arct. Cond., Ottawa, Canada: POAC, vol. 2; 2001. p. 669–82.

[9] Kärnä T, Qu Y. Analysis of the size effect in ice crushing – edition 1. VTT. Intern Rep; 2005.

[10] Timco GW, Irani MB, Tseng J, Liu LK, Zheng CB. Model tests of dynamic ice loading on the Chinese JZ-20-2 jacket platform. Can J Civ Eng 1992;19:819–32.

[11] Timco GW, Nwogu OG, Christensen FT. Compliant model tests with the Great Belt West Bridge piers in ice part I: Test methods and key results. Cold Reg Sci Technol 1995;23:149–64. https://doi.org/10.1016/0165-232X(94)00012-M.

[12] Christensen FT, Timco GW, Nwogu OG. Compliant model tests with the Great Belt West bridge piers in ice part II: Analyses of results. Cold Reg Sci Technol 1995;23: 165–82. https://doi.org/10.1016/0165-232X(94)00013-N.

[13] Cornett AM, Timco GW. Ice loads on an elastic model of the Molikpaq. Appl Ocean Res 1998;20:105–18. https://doi.org/10.1016/S0141-1187(98)00006-6.

[14] Sodhi DS. Crushing failure during ice-structure interaction. Eng Fract Mech 2001; 68:1889–921. https://doi.org/10.1016/S0013-7944(01)00038-8.

[15] Määttänen M. Laboratory tests for dynamic ice-structure interaction. In: Proc. Port Ocean Eng. under Arct. Cond., Trondheim, Norway: POAC; 1979. p. 1139–53.

[16] Toyama Y, Sensu T, Minami M, Yashima N. Model tests on ice-induced self-excited vibration of cylindrical structures. In: Proc. Int. Conf. Port Ocean Eng. under Arct. Cond., vol. 2, Helsinki, Finland: POAC; 1983. p. 834–44.

[17] Sodhi DS. Ice-structure interaction during indentation tests. Proc. IUTAM-IAHR Symp. Ice-structure Interact., St. John's, Newfoundland, Canada: Springer-Verlag

Berlin Heidelberg; 1991, p. 619–40. https://doi.org/10.1007/978-3-642-8
4100-2_31.

[18] Kärnä T, Muhonen A. Preliminary results from ice indentation tests using flexible and rigid indentors. In: Proc. 10th Int. Symp. Ice. Espoo/Helsinki, Finland: IAHR, vol. 3; 1990. p. 261–75.

[19] Kärnä T, Kolari K, Jochmann P, Evers K-U, Bi X. Tests on dynamic ice-structure interaction. In: Proc. 22nd Int. Conf. Offshore Mech. Arct. Eng., Cancún, Mexico: OMAE; 2003. p. 1–7.

[20] Yue Q, Guo F, Chu S. Laboratory tests of ice induced structure vibrations. In: Proc. 18th Int. Symp Ice.. Sapporo, Japan: IAHR, vol. 1; 2006. p. 191–8.

[21] Huang Y, Shi Q, Song A. Model test study of the interaction between ice and a compliant vertical narrow structure. Cold Reg Sci Technol 2007;49:151–60. https://doi.org/10.1016/j.coldregions.2007.01.004.

[22] Määttänen M, Løset S, Metrikine A, Evers K-U, Hendrikse H, Lønøy C, et al. Novel ice induced vibration testing in a large-scale facility: Deciphering ice induced vibrations, part 1. In: Proc. 21st Int. Symp. Ice. Dalian, China: IAHR; 2012. p. 946–58.

[23] Hendrikse H, Ziemer G, Owen CC. Experimental validation of a model for prediction of dynamic ice-structure interaction. Cold Reg Sci Technol 2018;151: 345–58.

[24] Passon P, Branner K, Larsen SE, Hvenekær JR. Offshore Wind Turbine Foundation Design. DTU Wind Energy PhD 2015;No. 0044(EN).

[25] Leppäranta M, Myrberg K. Physical Oceanography of the Baltic. Springer (ISBN: 978-3-540-79702-9).

[26] Leppäranta M. The Drift of Sea Ice. Springer (ISBN: 3-540-40881-9).

[27] Ervik Å, Nord TS, Høyland KV, Samardzija I, Li H. Ice-ridge interactions with the Norströmsgrund lighthouse: Global forces and interaction modes. Cold Reg Sci Technol 2019;158:195–220. https://doi.org/10.1016/j.coldregions.2018.08.020.

[28] Gedikli ED, Bjerkås M, Høyland KV, Hornnes V, Turner J. On the ice and wind conditions in the northern part of the Gulf of Bothnia leading ice-induced vibrations. Proc. 25th Int. Symp. Ice. Trondheim, Norway: 2020; p. 1–10.

[29] Yu S, Zhang D, Wang S, Wang G, Wang G, Yue Q, et al. Field monitoring of offshore wind turbine foundations in ice regions. J Coast Res 2020;104:343–50. https://doi.org/10.2112/JCR-SI104-063.1.

[30] Wang G, Zhang D, Yue Q, Yu S. Study on the dynamic ice load of offshore wind turbines with installed ice-breaking cones in cold regions. Energies 2022:15. https://doi.org/10.3390/en15093357.

[31] Kärnä KK, Tsukuda H. A numerical model for dynamic ice-structure interaction. Comput Struct 1999;72:645–58. https://doi.org/10.1016/S0045-7949(98)00337-X.

[32] Hendrikse H, Nord TS. Dynamic response of an offshore structure interacting with an ice floe failing in crushing. Mar Struct 2019;65:271–90. https://doi.org/10.1016/j.marstruc.2019.01.012.

[33] Barker A, Timco GW, Gravesen H, Vølund P. Ice loading on Danish wind turbines. Part 1: Dynamic model tests. Cold Reg Sci Technol 2005;41:1–23. https://doi.org/10.1016/j.coldregions.2004.05.002.

[34] Gravesen H, Sørensen SL, Vølund P, Barker A, Timco GW. Ice loading on Danish wind turbines: Part 2. Analyses of dynamic model test results. Cold Reg Sci Technol 2005;41:25–47. https://doi.org/10.1016/j.coldregions.2004.05.009.

[35] Ziemer G, Evers K. Ice model tests with a compliant cylindrical structure to investigate ice-induced vibrations. In: Proc. 33rd Int. Conf. Offshore Mech. Arct. Eng., San Fransisco, California, USA: OMAE; 2014. p. 1–8.

[36] Ji S, Yang D. Ice loads and ice-induced vibrations of offshore wind turbine based on coupled DEM-FEM simulations. Ocean Eng 2021:1–15. https://doi.org/10.1016/j.oceaneng.2021.110197.

[37] Tian Y, Huang Y, Li W. Experimental Investigations on Ice Induced Vibrations of a Monopile-type Offshore Wind Turbine in Bohai Sea. Proc. 29th Int. Ocean Polar Eng. Conf., Honolulu, Hawaii, USA: ISOPE 2019:327–34.

[38] Hammer TC, Willems T, Hendrikse H. Dynamic ice loads for offshore wind support structure design. Mar Struct 2022;87:103335. https://doi.org/10.1016/j.marstruc.2022.103335.

[39] Hendrikse H, Hammer TC, van den Berg M, Willems T, Owen CC, van Beek K, et al. Experimental data from ice basin tests with vertically sided cylindrical structures. Data Br 2022;41:1. https://doi.org/10.1016/j.dib.2022.107877.

[40] Hendrikse H, Hammer T, van den Berg M, Willems T, Owen C, van Beek K. Data from ice tank tests with vertically sided structures collected during the SHIVER project. 4TUResearchData Dataset 2021. https://doi.org/10.4121/17087462.v1.

[41] Hammer TC, Owen CC, van den Berg M, Hendrikse H. Classification of ice-induced vibrations regimes of offshore wind turbines. In: Proc. 41st Int. Conf. Offshore Mech. Arct. Eng. Hamburg, Germany: OMAE; 2022. p. 1–8. https://doi.org/10.1115/OMAE2022-78972.

[42] Palmer A, Dempsey J. Model tests in ice. Proc. 20th Int. Conf. Port Ocean Eng. under Arct. Cond., Luleå, Sweden: POAC; 2009.

[43] Ziemer G. Ice-Induced Vibrations of Vertical Structures. Tech Univ Hambg (Doctoral Thesis); 2021. https://doi.org/10.15480/882.4018.

[44] Hendrikse H, Hammer TC, Owen CC, Puolakka O, Willems T. Ice basin tests for ice-induced vibrations of offshore structures in the SHIVER project. In: Proc. 41st Int. Conf. Offshore Mech. Arct. Eng. Hamburg, Germany: OMAE; 2022. p. 1–9. https://doi.org/10.1115/OMAE2022-78507.

[45] McCrum DP, Williams MS. An overview of seismic hybrid testing of engineering structures. Eng Struct 2016;118:240–61. https://doi.org/10.1016/j.engstruct.2016.03.039.

[46] Hammer TC, Van BK, Koning J, Hendrikse H. A 2D test setup for scaled real-time hybrid tests of dynamic ice-structure interaction. Proc. 26th Int. Conf. Port Ocean Eng. under Arct. Cond., Moscow, Russia. POAC; 2021.

[47] International Electrotechnical Commission. Wind energy generation systems. IEC 61400-1 2019.

[48] Pereira D. Daniel Pereira. Wind Rose (https://www.mathworks.com/matlabcentral/fileexchange/47248-wind-rose), MATLAB Central File Exchange. Retrieved Jan 11, 2022. 2022.